

A Planar Carboxylate-Rich Tetrairon(II) Complex and Its Conversion to Linear Triiron(II) and Paddlewheel Diiron(II) Complexes

Erwin Reisner,[†] Joshua Telser,[‡] and Stephen J. Lippard^{*†}

Department of Chemistry, Massachusetts Institute of Technology, Cambridge, Massachusetts 02139, and Department of Biological, Chemical, and Physical Sciences, Roosevelt University, 430 S. Michigan Avenue, Chicago, Illinois 60605

Received August 23, 2007

We report a series of oligonuclear carboxylate-rich high-spin iron(II) complexes with three different $[\text{Fe}_n(\mu\text{-O}_2\text{Cbiph})_{2n}(\text{L})_m]$ ($n = 2\text{--}4$; $m = 2$ or 4) structural motifs, where O_2Cbiph is 2-biphenylcarboxylate and L is an exogenous ligand bound to terminal iron atoms. Solid compounds were isolated and their structural, spectroscopic, and magnetic properties thoroughly investigated. The discrete tetranuclear complexes $[\text{Fe}_4(\mu\text{-O}_2\text{Cbiph})_8(\text{L})_2]$ crystallize in a planar tetrairon(II) motif in which two diiron paddlewheel units are linked in an unprecedented manner involving a $\mu_3\text{-}1,1,3$ -bridging mode. X-ray crystallography reveals average $\text{Fe}\text{--}\text{O}_{\text{anti}}$ bond lengths of 2.081[2] Å at the dimer–dimer interface. Terminal axial positions are capped by ligands L, where L is tetrahydrofuran (THF) (**1**), indazole (**2**), pyrazole (**3**), 3,5-dimethylpyrazole (**4**), or acetamide (**5**). Reaction of **1** with an excess of acetonitrile affords the linear compound $[\text{Fe}_3(\mu\text{-O}_2\text{Cbiph})_6(\text{MeCN})_4]$ (**6**). The acetonitrile ligands in **6** can be replaced by THF or dimethoxyethane at elevated temperatures with retention of the structure to afford **7** and **8**, respectively. Reaction of **1** or **6** with pyridine or 1-methylimidazole results in the isolation of paddlewheel dimers **9** and **10**, respectively, with $[\text{Fe}_2(\mu\text{-O}_2\text{Cbiph})_4(\text{L})_2]$ composition. Mössbauer spectroscopy confirms the presence of high-spin ferrous ions and indicates that the two iron sites of the dimer are geometrically indistinguishable. For the tri- and tetrairon compounds, two quadrupole doublets are observed, suggesting that the iron centers do not have identical geometries. Plots of magnetic susceptibility versus temperature reveal intramolecular antiferromagnetic exchange coupling for all complexes under study. The magnetic data were fit to a theoretical model incorporating exchange coupling, single-ion zero-field splitting, and g -tensor anisotropy. The resulting magnetic parameters reveal in most cases weak antiferromagnetic exchange coupling (J typically $<3\text{ cm}^{-1}$) and dominant zero-field-splitting parameters.

Introduction

Metalloproteins with redox-active diiron cores coordinated to bridging carboxylate ligands are relatively common in biological systems. These diiron proteins perform multifaceted chemically and biologically intriguing functions including hydrocarbon oxidation and desaturation in bacterial multicomponent monooxygenases and stearyl–acyl carrier protein Δ^9 desaturase, respectively, radical generation in a class I ribonucleotide reductase R2 subunit, dioxygen transport in hemerythrin, and iron storage in ferritin.¹ There is much current interest in C–H bond activation,² stimulated in part by detailed investigations of methane hydroxylation by soluble methane monooxygenase (sMMO). The active

site of the hydroxylase component of this enzyme (MMOH) features a non-heme diiron center coordinated by four glutamate and two histidine residues. The reduced diiron(II) form (MMOH_{red}; Chart 1) reacts directly with dioxygen, activating it for methane hydroxylation.³

Recently, a variety of carboxylate-rich diiron(II) complexes have been prepared to mimic the active sites of non-heme

* To whom correspondence should be addressed. E-mail: lippard@mit.edu. Fax: 617-258-8150.

[†] Massachusetts Institute of Technology.

[‡] Roosevelt University.

- (1) (a) Lippard, S. J.; Berg, J. M. *Principles of Bioinorganic Chemistry*; University Science Books: Mill Valley, CA, 1994. (b) Bertini, I.; Gray, H. B.; Stiefel, E. I.; Valentine, J. S. *Biological Inorganic Chemistry: Structure and Reactivity*; University Science Books: Sausalito, CA, 2007.
- (2) (a) Bergman, R. G. *Nature* **2007**, *446*, 391–393. (b) Mas-Ballesté, R.; Que, L., Jr. *Science* **2006**, *312*, 1885–1886.
- (3) (a) Merckx, M.; Kopp, D. A.; Sazinsky, M. H.; Blazyk, J. L.; Müller, J.; Lippard, S. J. *Angew. Chem., Int. Ed.* **2001**, *40*, 2782–2807. (b) Sazinsky, M. H.; Lippard, S. J. *Acc. Chem. Res.* **2006**, *39*, 558–566. (c) Murray, L. J.; Lippard, S. J. *Acc. Chem. Res.* **2007**, *40*, 466–474. (d) Wallar, B. J.; Lipscomb, J. D. *Chem. Rev.* **1996**, *96*, 2625–2657.

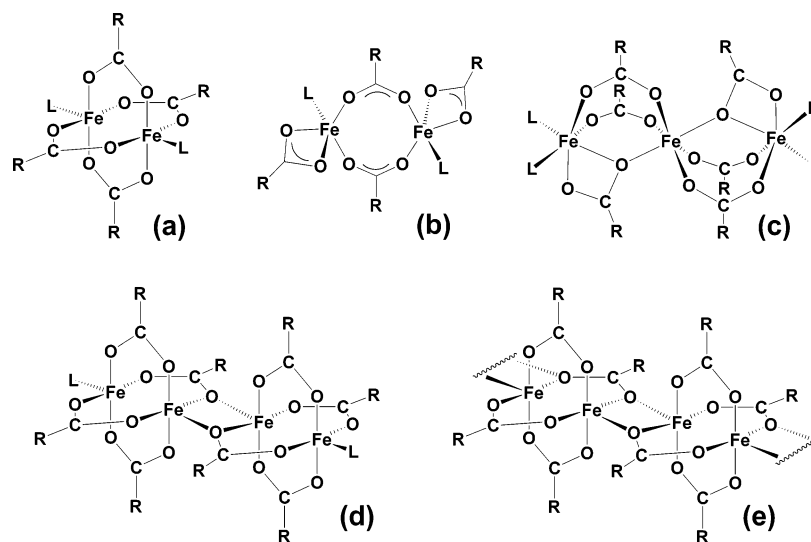
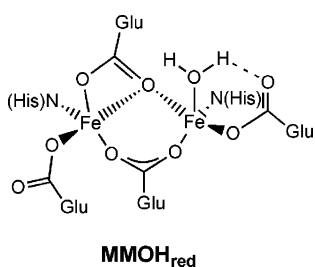


Figure 1. Oligonuclear structural motifs in carboxylate-rich ferrous complexes containing a $\{\text{Fe}_n(\text{O}_2\text{CR})_{2n}\}$ core: (a) diiron paddlewheel; (b) windmill; (c) linear triiron; (d) the unprecedented planar tetranuclear ferrous *dimer of dimers* motif; (e) the yet unreported corresponding polymeric assembly.

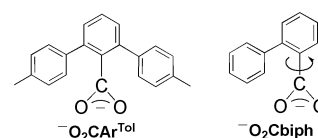
Chart 1



diiron centers like that in MMOH. The introduction of sterically hindered *m*-terphenyl-based carboxylates facilitates the assembly of discrete dinuclear cores with stoichiometries identical to that at the active site of the enzyme. These complexes emulate the hydrophobic protein active site cavity, and the bulky carboxylates prevent bimolecular decomposition of the assembled diiron(II) complexes. Diferrous complexes containing different *m*-terphenyl carboxylates and N-donor ligands display a variety of structural motifs; doubly bridged (windmill), triply bridged, and quadruply bridged (paddlewheel) diiron(II) complexes are commonly encountered (Figure 1a,b).⁴

Paddlewheel compounds such as $[\text{Fe}_2(\mu\text{-O}_2\text{CAR}^{\text{Tol}})_4\text{L}_2]$ ($\text{L} = 4\text{-cyano- or } 4\text{-acetylpyridine}$; $\text{O}_2\text{CAR}^{\text{Tol}} = 2,6\text{-di-}p\text{-tolylbenzoate}$; Chart 2) can convert to aquated windmill forms upon the addition of water to generate $[\text{Fe}_2(\mu\text{-O}_2\text{CAR}^{\text{Tol}})_2(\text{O}_2\text{CAR}^{\text{Tol}})_2\text{L}_2(\text{H}_2\text{O})_2]$ complexes. The oxygenation rates of the aquated windmill complexes are 10–20 times higher than those of their nonaquated paddlewheel analogues.⁵ Carboxylate-rich diiron(II) complexes have been successfully utilized in substrate oxidation by dioxygen, especially when the substrates are tethered to an N-donor

Chart 2



ligand such as pyridine, which facilitates the positioning of a functional group proximal to the diiron center. Sulfoxidation occurs in this manner and is controlled by the $\text{Fe}\cdots\text{S}$ distance; phosphine oxidation takes place only when the substrate is positioned in the ortho position of the pyridine ring.⁶

Because of the structural diversity of iron complexes with *m*-terphenylcarboxylate ligands, we were interested in investigating whether the sterically less demanding, asymmetric 2-biphenylcarboxylate O_2Cbiph (Chart 2) would provide sufficient steric bulk to avoid polymerization while maintaining the ability to facilitate the assembly of discrete oligonuclear iron(II) complexes with novel structural features and motifs. We speculated that the diminished steric crowding and possible rotation around the $\text{O}_2\text{C}-\text{C}_\alpha$ bond axis of the asymmetric carboxylate would enhance structural flexibility and possibly modulate the properties of the resulting constructs. Here we describe the use of O_2Cbiph to prepare a planar tetranuclear $[\text{Fe}_4(\mu\text{-O}_2\text{Cbiph})_8(\text{THF})_2]$ (THF = tetrahydrofuran) complex with a *dimer of dimers* structure, the geometry of which is unprecedented in iron chemistry. The tetranuclear construct can be converted into linear triiron(II) and paddlewheel diiron(II) complexes having $[\text{Fe}_n(\mu\text{-O}_2\text{Cbiph})_{2n}(\text{L})_m]$ ($n = 2\text{--}4$; $m = 2$ or 4) stoichiometries. The syntheses, structures, spectroscopic and magnetic properties, and interconversion chemistry of these compounds are discussed in detail.

(4) (a) Tshuva, E. Y.; Lippard, S. J. *Chem. Rev.* **2004**, *104*, 987–1012. (b) Tolman, W. B.; Que, L., Jr. *J. Chem. Soc., Dalton Trans.* **2002**, 653–660. (c) Lee, D.; Lippard, S. J. In *Comprehensive Coordination Chemistry II*; McCleverty, J., Meyer, T. J., Eds.; Elsevier: Oxford, U.K., 2003; Vol. 8, pp 309–342. (5) (a) Yoon, S.; Lippard, S. J. *J. Am. Chem. Soc.* **2005**, *127*, 8386–8397. (b) Zhao, M.; Song, D.; Lippard, S. J. *Inorg. Chem.* **2006**, *45*, 6323–6330.

(6) (a) Carson, E. C.; Lippard, S. J. *J. Am. Chem. Soc.* **2004**, *126*, 3412–3413. (b) Carson, E. C.; Lippard, S. J. *Inorg. Chem.* **2006**, *45*, 828–836. (c) Carson, E. C.; Lippard, S. J. *Inorg. Chem.* **2006**, *45*, 837–848. (d) Reisner, E.; Abikoff, T. C.; Lippard, S. J. *Inorg. Chem.* **2007**, in press. (e) Yoon, S.; Lippard, S. J. *Inorg. Chem.* **2006**, *45*, 5438–5446.

Experimental Section

General Considerations. All reagents were obtained from commercial suppliers and used as received unless otherwise noted. Dichloromethane, tetrahydrofuran (THF), and pentane used for the preparation of the iron(II) complexes were saturated with dinitrogen and purified by passage through activated Al_2O_3 columns under argon.⁷ Anhydrous dimethoxyethane was purchased from Aldrich and deoxygenated by bubbling argon through the solution prior use. Chlorobenzene (distilled over P_4O_{10}) and acetonitrile (predried over molecular sieves and distilled over CaH_2) were freshly dried prior to use. Sodium hydroxide pellets were ground and dried at 40 °C under high vacuum overnight. $\text{Fe}(\text{OTf})_2 \cdot 2\text{MeCN}$ was prepared according to a literature procedure.⁸ All ferrous complexes were prepared under dinitrogen in an Mbraun drybox.

Physical Measurements. ^1H and ^{13}C NMR spectra were measured with a Varian 300 or 500 MHz spectrometer at the MIT Department of Chemistry Instrumentation Facility. Chemical shifts were referenced to residual solvent peaks.⁹ Electrospray ionization mass spectrometry (ESI-MS) spectra were obtained in methanol solutions with an Agilent 1100 series LC/MSD mass spectrometer. Fourier transform IR spectra were recorded on a Thermo Nicolet Avatar 360 spectrometer with the *OMNIC* software. UV–vis spectra were recorded on a Hewlett-Packard 8453 diode array spectrophotometer under anaerobic conditions. Melting points were measured on an electrothermal Mel-Temp melting point apparatus. When compounds were prepared by two different methods, the composition of the material synthesized by Method 2 was confirmed by IR spectroscopy and by a unit cell determination of the crystalline material.

Synthesis. Sodium 2-Biphenylcarboxylate (NaO_2biph). 2-Biphenylcarboxylic acid (1.50 g, 7.57 mmol) and sodium hydroxide (0.31 g, 7.57 mmol) in MeOH (40 mL) were heated at 50 °C for 3 h. The solution was cooled to room temperature, concentrated to dryness, and kept at 60 °C overnight under high vacuum. Yield: 1.67 g, quant. ^1H NMR (300 MHz, CD_3OD) δ : 7.54 (dt, $J = 6.9$ and 1.8 Hz, 2H); 7.48 (dt, $J = 6.3$ and 1.5 Hz, 1H); 7.38–7.23 (m, 6H). ^{13}C NMR (300 MHz, CD_3OD) δ : 179.2, 143.4, 142.7, 140.0, 130.9, 129.8, 129.2, 128.9, 128.2, 127.9, 127.9. Mp: >300 °C. ESI-MS (m/z , MeOH). Calcd for $[\text{M} - \text{Na}]^-$ 197.1, $[2\text{M} - \text{Na}]^-$ 417.1, $[3\text{M} - \text{Na}]^-$ 637.2, $[4\text{M} - \text{Na}]^-$ 857.2. Found: 196.9 (4%), 417.0 (23%), 637.1 (80%), 857.1 (100%). IR (KBr): 3067 (m), 3022 (w), 2963 (w), 1601 (m), 1584 (s), 1572 (s), 1560 (s), 1475 (w), 1448 (w), 1436 (w), 1408 (s), 1391 (m), 1262 (m), 1101 (w), 1074 (w), 1009 (w), 848 (w), 812 (w), 778 (w), 746 (s), 702 (m), 664 (m), 615 (w), 518 (w), 407 (w).

$[\text{Fe}_4(\mu_3\text{-O}_2\text{Cbiph})_2(\mu_2\text{-O}_2\text{Cbiph})_6(\text{THF})_2]$ (1). Method 1. A portion of $\text{Fe}(\text{OTf})_2 \cdot 2\text{MeCN}$ (500 mg, 1.15 mmol) and NaO_2Cbiph (505 mg, 2.29 mmol) were suspended in THF (15 mL) and stirred at room temperature. After 15 min, an olive-green solution was formed, which was concentrated to dryness after 2 h under reduced pressure at room temperature. The product was then extracted into CH_2Cl_2 (10 mL). A white solid (NaOTf) was filtered off, and the product was recrystallized from CH_2Cl_2 by pentane vapor diffusion. After 4 days, the green crystals that formed were washed with pentane and dried under high vacuum at room temperature. Yield: 522 mg (47%). X-ray diffraction quality single crystals were selected directly from the reaction vessel. Anal. Calcd for **1**,

$\text{C}_{112}\text{H}_{88}\text{O}_{18}\text{Fe}_4$ ($M_r = 1945.31 \text{ g mol}^{-1}$): C, 69.15; H, 4.56. Found: C, 68.93; H, 4.42. Mp: 131–134 °C (dec). IR (KBr): 3054 (m), 3022 (m), 2976 (w), 1945 (w), 1617 (s), 1479 (m), 1449 (m), 1438 (m), 1416 (s), 1264 (w), 1264 (m), 1103 (w), 1075 (m), 1051 (w), 1032 (m), 1018 (m), 1008 (m), 918 (m), 859 (s), 844 (m), 776 (m), 747 (s), 700 (s), 665 (s), 523 (s), 477 (m), 453 (m).

Method 2. Powdered yellow crystals of $[\text{Fe}_3(\text{O}_2\text{Cbiph})_6(\text{MeCN})_4]$ (**6**; 100 mg, 65 μmol) were dissolved in THF (5 mL), and the resulting green solution was stirred for 30 min. The solution was concentrated to dryness and the crude product recrystallized from CH_2Cl_2 by pentane vapor diffusion. The colorless–green dichroic blocks were washed with pentane and dried under high vacuum. Yield: 80 mg (80%).

$[\text{Fe}_4(\mu_3\text{-O}_2\text{Cbiph})_2(\mu_2\text{-O}_2\text{Cbiph})_6(\text{indazole})_2]$ (2). Indazole (11.8 mg, 100 μmol) dissolved in CH_2Cl_2 (2 mL) was added to a stirred yellow solution of **6** (100 mg, 65 μmol) in CH_2Cl_2 (6 mL). The resulting pale-green solution was stirred for 30 min, and the product was crystallized by pentane vapor diffusion to give colorless–green dichroic blocks within several days. The crystals were washed with pentane and dried under high vacuum. Yield: 72 mg (69%). X-ray diffraction quality single crystals were selected directly from the reaction vessel, yielding $2 \cdot 2\text{CH}_2\text{Cl}_2$. Anal. Calcd for $2 \cdot \text{CH}_2\text{Cl}_2$, $\text{C}_{119}\text{H}_{86}\text{Cl}_2\text{Fe}_4\text{N}_4\text{O}_{16}$ ($M_r = 2122.26 \text{ g mol}^{-1}$): C, 67.35; H, 4.08; N, 2.64. Found: C, 67.37; H, 4.21; N, 2.82. Mp: 92–94 °C (dec). IR (KBr): 3401 (m), 3054 (m), 3021 (w), 2922 (s), 2851 (w), 1608 (s), 1590 (s), 1573 (m), 1557 (m), 1478 (m), 1450 (w), 1437 (m), 1401 (s), 1267 (w), 1154 (w), 1100 (w), 1074 (w), 1051 (w), 1008 (m), 955 (m), 859 (m), 844 (m), 777 (m), 745 (s), 699 (s), 664 (s), 521 (m), 469 (m).

$[\text{Fe}_4(\mu_3\text{-O}_2\text{Cbiph})_2(\mu_2\text{-O}_2\text{Cbiph})_6(\text{pyrazole})_2]$ (3). **6** (100 mg, 65 μmol) was dissolved in CH_2Cl_2 (4 mL), and pyrazole (6.7 mg, 99 μmol) dissolved in CH_2Cl_2 (4 mL) was added to the stirred yellow solution. After 30 min, the pale-green solution was set up for crystallization by pentane vapor diffusion to give green–colorless dichroic crystals within several days, which were washed with pentane and dried under high vacuum. Yield: 78 mg (80%). X-ray diffraction quality single crystals were selected directly from the reaction vessel. Anal. Calcd for $3 \cdot \frac{1}{2}\text{CH}_2\text{Cl}_2$, $\text{C}_{110.5}\text{H}_{81}\text{ClFe}_4\text{N}_4\text{O}_{16}$ ($M_r = 1979.68 \text{ g mol}^{-1}$): C, 67.04; H, 4.12; N, 2.83. Found: C, 67.10; H, 3.93; N, 2.82. Mp: 114–117 °C (dec). IR (KBr): 3367 (m), 3054 (m), 3021 (w), 1607 (s), 1591 (m), 1571 (w), 1479 (m), 1449 (m), 1440 (m), 1395 (s), 1349 (w), 1155 (m), 1057 (m), 1043 (m), 1008 (m), 859 (m), 845 (m), 776 (m), 745 (s), 700 (s), 666 (s), 523 (m), 453 (m).

$[\text{Fe}_4(\mu_3\text{-O}_2\text{Cbiph})_2(\mu_2\text{-O}_2\text{Cbiph})_6(3,5\text{-dimethylpyrazole})_2]$ (4). **6** (100 mg, 65 μmol) was dissolved in CH_2Cl_2 (5 mL), and 3,5-dimethylpyrazole (9.5 mg, 99 μmol) dissolved in CH_2Cl_2 (3 mL) was added dropwise to the stirred yellow solution. After 30 min, the pale-green solution was set aside for crystallization by pentane vapor diffusion to give large green blocks within several days. The crystals were washed with pentane and dried under high vacuum. Yield: 68 mg (66%). X-ray diffraction quality single crystals were selected directly from the reaction vessel, yielding $4\text{a} \cdot 4\text{CH}_2\text{Cl}_2$ and $4\text{b} \cdot 2\text{CH}_2\text{Cl}_2$. Anal. Calcd for $4 \cdot \text{CH}_2\text{Cl}_2$, $\text{C}_{115}\text{H}_{90}\text{N}_4\text{Cl}_2\text{Fe}_4\text{O}_{16}$ ($M_r = 2078.25 \text{ g mol}^{-1}$): C, 66.46; H, 4.36; N, 2.70. Found: C, 66.48; H, 4.08; N, 2.92. Mp: 88–90 °C (dec). IR (KBr): 3342 (m), 3057 (m), 3020 (m), 2920 (w), 1611 (s), 1590 (m), 1570 (m), 1475 (m), 1450 (w), 1438 (w), 1403 (s), 1279 (w), 1264 (w), 1036 (w), 1008 (w), 777 (m), 746 (s), 699 (s), 664 (s), 518 (m), 464 (m).

$[\text{Fe}_4(\mu_3\text{-O}_2\text{Cbiph})_2(\mu_2\text{-O}_2\text{Cbiph})_6(\text{acetamide})_2]$ (5). **6** (100 mg, 65 μmol) was dissolved in acetonitrile (5 mL), and acetamide (6.9 mg, 99 μmol) was added to the stirred yellow solution. After 2 h, the product was stripped to dryness and the solid was recrystallized

(7) Pangborn, A. B.; Giardello, M. A.; Grubbs, R. H.; Rosen, R. K.; Timmers, F. J. *Organometallics* **1996**, *15*, 1518–1520.

(8) Hagen, K. S. *Inorg. Chem.* **2000**, *39*, 5867–5869.

(9) Gottlieb, H. E.; Kotlyar, V.; Nudelman, A. *J. Org. Chem.* **1997**, *62*, 7512–7515.

from chlorobenzene by pentane vapor diffusion. After several days, the resulting yellow–green dichroic blocks were washed with pentane and dried under high vacuum. Yield: 48 mg (51%). X-ray diffraction quality single crystals were selected directly from the reaction vessel, yielding **5**·2C₇H₅Cl. Anal. Calcd for **5**, C₁₀₈H₈₂N₂·Fe₄O₁₈ ($M_r = 1919.19 \text{ g mol}^{-1}$): C, 67.59; H, 4.31; N, 1.46. Found: C, 67.95; H, 4.32; N, 1.56. Mp: 108–113 °C (dec). IR (KBr): 3478 (m), 3056 (m), 3021 (w), 2929 (w), 1606 (s), 1588 (s), 1575 (m), 1478 (m), 1450 (m), 1439 (m), 1408 (s), 1266 (w), 1153 (w), 1078 (w), 1020 (w), 1008 (w), 775 (w), 746 (s), 700 (s), 664 (m), 601 (w), 515 (m), 469 (m).

[Fe₃(μ₃-O₂Cbiph)₂(μ₂-O₂Cbiph)₄(MeCN)₄] (**6**). Acetonitrile (8 mL) was added to a stirred green suspension of **1** (200 mg, 103 μmol) in CH₂Cl₂ (4 mL). The reaction mixture was heated at 40 °C for ca. 5 min until an intense yellow solution was formed, which was allowed to stand at room temperature. Yellow blocks of the product were isolated after 4 days, and the crystals were washed with pentane. Yield: 174 mg (83%). X-ray diffraction quality single crystals were selected directly from the reaction vessel, yielding **6a** and **6b**·CH₂Cl₂. Anal. Calcd for **6**·0.25CH₂Cl₂, C_{86.25}H_{66.5}Cl_{0.5}·Fe₃N₄O₁₂ ($M_r = 1536.23 \text{ g mol}^{-1}$): C, 67.43; H, 4.36; N, 3.65. Found: C, 67.49; H, 4.27; N, 3.45. Mp: 89–92 °C (dec). IR (KBr): 3053 (m), 3019 (w), 2988 (w), 2928 (w), 2304 (m), 2276 (m), 1606 (s), 1592 (s), 1576 (w), 1530 (m), 1479 (w), 1450 (w), 1437 (w), 1400 (s), 1155 (w), 1076 (w), 1008 (w), 864 (w), 807 (w), 778 (m), 745 (s), 728 (m), 702 (s), 662 (m), 516 (m).

[Fe₃(μ₃-O₂Cbiph)₂(μ₂-O₂Cbiph)₄(THF)₄] (**7**). Powdered yellow crystals of **6** (50 mg, 33 μmol) were dissolved in THF (4 mL), and the solution was gently heated to boiling for 2 min. The resulting yellow solution was layered with pentane. After several days, yellow blocks were isolated and washed with pentane. X-ray diffraction quality single crystals were selected directly from the reaction vessel. Yield: 38 mg (69%). Anal. Calcd for **7**·0.25CH₂Cl₂, C_{94.25}H_{86.5}Cl_{0.5}Fe₃O₁₆ ($M_r = 1660.45 \text{ g mol}^{-1}$): C, 68.18; H, 5.25. Found: C, 67.94; H, 5.04. Mp: 93–97 °C (dec). IR (KBr): 3056 (m), 3022 (w), 2975 (m), 2874 (m), 1604 (s), 1590 (s), 1576 (w), 1478 (m), 1449 (m), 1437 (m), 1402 (s), 1262 (w), 1155 (w), 1036 (m), 1008 (w), 876 (w), 778 (w), 745 (s), 700 (s), 663 (m), 519 (w), 443 (w).

[Fe₃(μ₃-O₂Cbiph)₂(μ₂-O₂Cbiph)₄(DME)₂] (**8**). **Method 1.** **6** (100 mg, 65 μmol) was dissolved in MeCN (8 mL), dimethoxyethane (8 mL), and CH₂Cl₂ (4 mL) under gentle heating. The resulting yellow solution was allowed to cool slowly to room temperature, and the yellow diamond-shaped blocks that formed within several days were washed with pentane and dried under high vacuum. Yield: 68 mg (67%). X-ray diffraction quality single crystals were selected directly from the reaction vessel. Anal. Calcd for **8**, C₈₆H₇₄·Fe₃O₁₆ ($M_r = 1531.03 \text{ g mol}^{-1}$): C, 67.47; H, 4.87. Found: C, 67.04; H, 4.82. Mp: 111–113 °C (dec). IR (KBr): 3060 (w), 3019 (w), 2941 (w), 1590 (s), 1577 (m), 1479 (m), 1451 (m), 1401 (s), 1101 (m), 1065 (m), 1009 (m), 862 (m), 779 (w), 742 (s), 698 (m), 662 (m), 513 (w).

Method 2. A solution of **1** (50 mg, 26 μmol) was stirred for 10 min in MeCN (4 mL), after which dimethoxyethane (4 mL) was added to the reaction mixture. After 5 min, the yellow suspension was heated at 50 °C and the resulting yellow solution was allowed to cool slowly to room temperature. The yellow blocks formed were washed with pentane and dried under high vacuum. Yield: 42 mg (80%).

[Fe₂(μ₂-O₂Cbiph)₄(py)₂] (**9**). **Method 1.** Pyridine (12 mg, 152 μmol) in CH₂Cl₂ (2 mL) was added dropwise to a stirred suspension of **1** (49 mg, 25 μmol) in CH₂Cl₂ (7 mL) at room temperature. After 1 h, the resulting yellow solution was exposed to pentane

vapor diffusion. Several days later, the yellow crystals that formed were washed with pentane and dried at room temperature under high vacuum. Yield: 49 mg (86%). X-ray diffraction quality single crystals were selected directly from the reaction vessel, yielding **9**·CH₂Cl₂. Anal. Calcd for **9**·CH₂Cl₂, C₆₃H₄₈N₂Cl₂O₈Fe₂ ($M_r = 1143.66 \text{ g mol}^{-1}$): C, 66.16; H, 4.23; N, 2.45. Found: C, 66.32; H, 4.03; N, 2.44. ¹H NMR (500 MHz, CD₂Cl₂) δ: 93.1, 29.6, 14.2, 13.0, 10.0, 7.8, 7.4, 6.2, 4.9, 4.6. Mp: 133–136 °C (dec). IR (KBr): 3053 (m), 3014 (m), 1622 (s), 1601 (s), 1566 (m), 1477 (m), 1445 (s), 1397 (s), 1268 (w), 1211 (w), 1150 (w), 1068 (m), 1042 (m), 1002 (m), 841 (m), 781 (m), 763 (s), 748 (s), 715 (m), 695 (s), 664 (s), 549 (m). UV–vis [CH₂Cl₂, λ_{max}, nm (ε, M⁻¹ cm⁻¹): 374 (1900).

Method 2. Pyridine (12 mg, 152 μmol) in CH₂Cl₂ (1 mL) was added dropwise to a stirred suspension of **6** (50 mg, 33 μmol) in CH₂Cl₂ (3 mL) at room temperature. After 30 min, the yellow solution was exposed to pentane vapor diffusion. Yellow crystals formed after 2 days and were washed with pentane and dried at room temperature under high vacuum. Yield: 50 mg (88%).

[Fe₂(μ₂-O₂Cbiph)₄(1-MeIm)₂] (**10**). 1-Methylimidazole (12 mg, 146 μmol) in CH₂Cl₂ (2 mL) was added to a stirred suspension of **1** (49 mg, 25 μmol) in CH₂Cl₂ (5 mL). After 30 min, the resulting yellow solution was carefully layered with pentane (3 mL) and allowed to stand for crystallization. Yellow crystals were harvested after 3 days, washed with pentane, and dried at room temperature. Yield: 48 mg (88%). X-ray diffraction quality single crystals were selected directly from the reaction vessel, yielding **10**·CH₂Cl₂. Anal. Calcd for **10**·0.25CH₂Cl₂, C_{60.25}H_{48.5}Cl_{0.5}N₄Fe₂O₈ ($M_r = 1085.97 \text{ g mol}^{-1}$): C, 66.64; H, 4.50; N, 5.16. Found: C, 66.37; H, 4.31; N, 5.09. ¹H NMR (500 MHz, CD₂Cl₂) δ: 29.8, 23.6, 20.2, 13.9, 13.6, 10.6, 9.6, 7.4, 5.9, 5.0, 1.3, 0.9. Mp: 110–112 °C (dec). IR (KBr): 3128 (m), 3044 (m), 3014 (m), 1629 (s), 1594 (m), 1533 (m), 1477 (m), 1436 (m), 1394 (s), 1281 (w), 1233 (w), 1111 (s), 1091 (m), 1008 (m), 947 (m), 843 (s), 748 (s), 699 (s), 664 (s), 617 (m).

X-ray Crystallographic Studies. Intensity data were recorded on a Bruker APEX CCD diffractometer with graphite-monochromated Mo Kα radiation (λ = 0.710 73 Å), controlled by a Pentium-based PC running the SMART software package.¹⁰ Single crystals were mounted in Paratone N oil on the tips of glass fibers or loops and cooled under a stream of dinitrogen maintained by a KRYO-FLEX low-temperature apparatus. A total of 2800 frames were measured for each compound. The structures were solved by direct methods for **1–5** and **9–11** and by the Patterson method for **6–8** and were refined on F^2 by using the SHELXTL software package.¹¹ Empirical absorption corrections were applied with SADABS,¹² and the structures were validated using the PLATON software.¹³ All non-hydrogen atoms were located, and their positions were refined with anisotropic thermal parameters. Hydrogen atoms were placed at calculated positions, except the two amide protons in **5**, which were located in the difference Fourier map. Hydrogen atoms were assigned thermal parameters equal to either 1.5 (methyl hydrogen atoms) or 1.2 (non-methyl hydrogen atoms) times the thermal parameters of the atom to which they were attached.

(10) SMART, Software for the CCD Detector System, version 5.6; Bruker AXS: Madison, WI, 2000.

(11) (a) Sheldrick, G. M. SHELXTL00: Program for Refinement of Crystal Structures; University of Göttingen: Göttingen, Germany, 2000. (b) SHELXTL, Program Library for Structure Solution and Molecular Graphics, version 6.10; Bruker AXS: Madison, WI, 2001.

(12) Sheldrick, G. M. SADABS: Area-Detector Absorption Correction; University of Göttingen: Göttingen, Germany, 2001.

(13) Spek, A. L. PLATON, A Multipurpose Crystallographic Tool; Utrecht University: Utrecht, The Netherlands, 2000.

Table 1. Crystal Data and Details of Data Collection for Compounds **1–5**

	1	2·2CH₂Cl₂	3	4a·4CH₂Cl₂	5·2C₆H₅Cl
chemical formula	C ₁₁₂ H ₈₈ Fe ₄ O ₁₈	C ₁₂₀ H ₈₈ Cl ₄ Fe ₄ N ₄ O ₁₆	C ₁₁₀ H ₈₀ Fe ₄ N ₄ O ₁₆	C ₁₁₈ H ₉₆ Cl ₈ Fe ₄ N ₄ O ₁₆	C ₁₂₀ H ₉₂ Cl ₂ Fe ₄ N ₂ O ₁₈
fw (g mol ⁻¹)	1945.27	2207.14	1937.18	2332.99	2144.26
space group	<i>P</i> 2 ₁ / <i>n</i>	<i>P</i> 1	<i>P</i> 2 ₁ / <i>n</i>	<i>P</i> 1	<i>P</i> 1
<i>a</i> (Å)	13.1530(19)	14.0208(15)	13.559(6)	13.2698(7)	13.955(3)
<i>b</i> (Å)	25.159(4)	14.2725(15)	24.633(11)	13.7009(7)	14.181(3)
<i>c</i> (Å)	14.097(2)	15.7331(16)	13.817(6)	29.8852(16)	15.806(3)
α (deg)		109.966(2)		93.2150(10)	109.421(3)
β (deg)	93.854(3)	96.596(2)	96.444(9)	94.7490(10)	95.956(3)
γ (deg)		115.812(2)		91.0210(10)	116.237(3)
<i>V</i> (Å ³)	4654.3(12)	2531.4(5)	4586(4)	5404.8(5)	2527.1(9)
<i>Z</i>	2	1	2	2	1
ρ _{calc} (g cm ⁻³)	1.388	1.448	1.403	1.434	1.409
cryst size (mm)	0.25 × 0.25 × 0.20	0.30 × 0.25 × 0.20	0.16 × 0.14 × 0.12	0.40 × 0.40 × 0.40	0.18 × 0.12 × 0.12
<i>s</i> frame ⁻¹	10	10	10	5	10
<i>T</i> (K)	110	110	110	110	110
λ(Mo Kα) (mm ⁻¹)	0.683	0.739	0.692	0.792	0.688
Θ range (deg)	2.17–27.88	2.08–25.68	2.16–25.02	2.12–27.10	2.08–26.37
total no. of data	79 075	37 310	63 384	87 883	39 327
no. of unique data	11 104	9579	8106	23 695	10 295
no. of param	604	667	604	1380	665
completeness to θ (%)	100	99.6	99.9	99.4	99.6
R1 ^a	0.0414	0.0434	0.0463	0.0345	0.0495
wR2 ^b	0.0944	0.1075	0.0995	0.0817	0.1015
GOF ^c	1.131	1.038	1.026	1.029	1.044

^a R1 = $\sum||F_o| - |F_c||/\sum|F_o|$. ^b wR2 = $\{\sum[w(F_o^2 - F_c^2)^2]/\sum[w(F_o^2)^2]\}^{1/2}$. ^c GOF = $\{\sum[w(F_o^2 - F_c^2)^2]/(n - p)\}^{1/2}$, where *n* is the number of reflections and *p* is the total number of parameters refined.

Table 2. Crystal Data and Details of Data Collection for Compounds **6–10**

	6a	7	8	9·CH₂Cl₂	10·CH₂Cl₂
chemical formula	C ₈₆ H ₆₆ Fe ₃ N ₄ O ₁₂	C ₉₄ H ₈₆ Fe ₃ O ₁₆	C ₈₆ H ₇₄ Fe ₃ O ₁₆	C ₆₃ H ₄₈ Cl ₂ Fe ₂ N ₂ O ₈	C ₆₁ H ₅₀ Cl ₂ Fe ₂ N ₄ O ₈
fw (g mol ⁻¹)	1514.98	1639.18	1530.98	1143.63	1149.6
space group	<i>P</i> 1	<i>P</i> 1	<i>P</i> 1	<i>C</i> 2/ <i>c</i>	<i>C</i> 2/ <i>c</i>
<i>a</i> (Å)	12.598(2)	13.776(2)	12.222(13)	24.960(7)	24.769(10)
<i>b</i> (Å)	12.617(2)	14.849(2)	12.345(9)	10.012(3)	10.586(6)
<i>c</i> (Å)	13.368(2)	22.949(5)	13.650(11)	21.217(6)	20.607(10)
α (deg)	71.827(3)	94.328(4)	104.55(2)		
β (deg)	83.311(3)	105.652(3)	115.45(2)	92.282(5)	91.00(4)
γ (deg)	64.997(3)	117.224(2)	90.96(3)		
<i>V</i> (Å ³)	1829.3(5)	3909.6(11)	1782(3)	5298(3)	5402(4)
<i>Z</i>	1	2	1	4	4
ρ _{calc} (g cm ⁻³)	1.375	1.392	1.427	1.434	1.414
cryst size (mm)	0.40 × 0.20 × 0.10	0.32 × 0.24 × 0.10	0.30 × 0.10 × 0.05	0.35 × 0.25 × 0.25	0.40 × 0.30 × 0.04
<i>s</i> frame ⁻¹	10	7	10	7	10
<i>T</i> (K)	110	110	110	110	110
λ(Mo Kα) (mm ⁻¹)	0.654	0.620	0.675	0.709	0.697
Θ range (deg)	2.07–25.68	2.10–26.37	2.35–27.91	2.19–27.88	2.09–27.02
total no. of data	26 938	60 798	30 602	44 243	42 158
no. of unique data	6924	15 918	8407	6321	5907
no. of param	477	1036	477	348	350
completeness to θ (%)	99.6	99.5	98.8	100	99.8
R1 ^a	0.0381	0.0417	0.0415	0.0328	0.0386
wR2 ^b	0.0988	0.0954	0.0916	0.0804	0.0916
GOF ^c	1.046	1.022	1.065	1.081	1.120

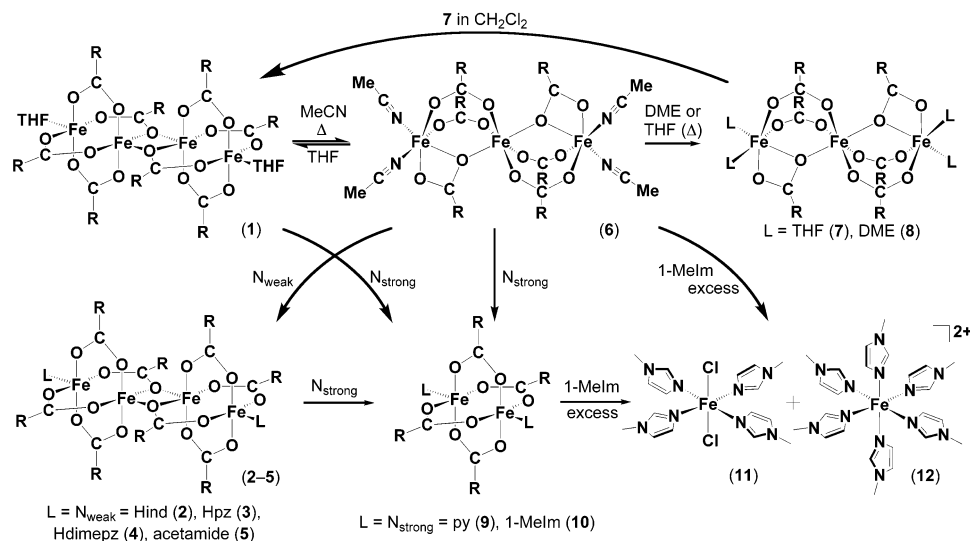
^a R1 = $\sum||F_o| - |F_c||/\sum|F_o|$. ^b wR2 = $\{\sum[w(F_o^2 - F_c^2)^2]/\sum[w(F_o^2)^2]\}^{1/2}$. ^c GOF = $\{\sum[w(F_o^2 - F_c^2)^2]/(n - p)\}^{1/2}$, where *n* is the number of reflections and *p* is the total number of parameters refined.

X-ray diffraction quality single crystals were selected directly from the reaction vessels. Complex **2** contains two CH₂Cl₂ solvent molecules per tetrairon unit. Polymorphism was encountered when mounting several crystals of **4** and **6**. Complex **4a** crystallizes with four CH₂Cl₂ molecules per tetranuclear unit, of which one is disordered over two positions, and **4b** contains one disordered 2-biphenylcarboxylate ligand with one CH₂Cl₂ solvent molecule per asymmetric unit. Compound **6a** contains half a molecule of the complex in the asymmetric unit, and no solvent molecules could be located. Two half-molecules were identified in the asymmetric unit of **6b**, which contains one CH₂Cl₂ molecule per triiron unit. One fully occupied chlorobenzene solvent molecule per asymmetric unit was encountered in **5**. One phenyl ring in **9** is involved in 1:1

positional disorder. In **9** and **10**, one dichloromethane half-molecule lies on a center of symmetry, resulting in one solvent molecule per complex in the crystal lattice of these compounds. No solvent molecules were located in the crystal lattices of **1**, **3**, **7**, **8**, and **11**. Crystal data, data collection parameters, and structure refinement details for **1–10** are given in Tables 1 and 2 and those for **4b**, **6b** and **11** in the Supporting Information. ORTEP diagrams, atom-labeling schemes, CIF files, and tables containing interatomic distances and angles for complexes **1–11** can be found in the Supporting Information.

⁵⁷Fe Mössbauer Spectroscopy. Zero-field Mössbauer spectra were obtained on an MS1 spectrometer (WEB Research Co.) with a ⁵⁷Co source in a rhodium matrix maintained at room

Scheme 1



temperature housed in the MIT Department of Chemistry. Solid samples were prepared by suspending powdered samples in Apiezon grease and packing the mixture into a nylon sample holder. All samples were prepared and loaded in an Mbraun glovebox and transported to the spectrometer in liquid nitrogen. All data were collected at 4.2 K, and the isomer shift (δ) values are reported with respect to natural iron foil that was used for velocity calibration at room temperature. Spectra were fit by using the *WMOSS* program.¹⁴

Magnetic Susceptibility Studies. Magnetic susceptibility data for polycrystalline powders of the complexes were measured between 2 and 300 K at the MIT Center for Materials Science and Engineering on a Quantum Design MPMS-5S SQUID susceptometer in direct current mode. In a typical experiment, magnetic fields of 0.1, 10, and 50 kOe were applied and 82 data points were collected per temperature sweep. No temperature-dependent hysteresis was observed for any of the compounds when collecting data during the warm-up or cool-down periods. Samples were loaded into capsules in a glovebox and mounted in a plastic straw under a dinitrogen atmosphere. The samples were transported to the susceptometer in liquid nitrogen, and care was taken to minimize exposure to air. On several occasions, samples were examined for color changes in a glovebox and analyzed by ⁵⁷Fe Mössbauer spectroscopy following magnetic measurements. In no case could significant oxidation impurities be detected. Data were corrected for the magnetism of the sample holder, which was independently determined at the same temperature range and fields. The underlying diamagnetism of the samples was subtracted from the experimental susceptibilities and estimated by using Pascal's constants.¹⁵ The values were calculated to be -1.12×10^{-3} (2), -1.05×10^{-3} (3), -1.10×10^{-3} (4), -8.08×10^{-4} (6), -8.55×10^{-4} (8), -5.87×10^{-4} (9), and -5.91×10^{-4} (10) $\text{cm}^3 \text{mol}^{-1}$.

Magnetic Susceptibility Fitting Methodology. Magnetic susceptibility data were fit by using locally written programs that involved solving the spin Hamiltonian matrix for Fe^{II}_n ($n = 1-4$) systems.^{16,17} The procedure involved simultaneous best fits to

variable-temperature susceptibility data collected at several magnetic fields. A standard spin Hamiltonian for coupled spin systems was employed, which includes, in order of increasing interaction energy, anisotropic electronic Zeeman coupling to each Fe^{II} spin, zero-field splitting (zfs) for each Fe^{II} , and anisotropic exchange coupling between the two to four electronic spins.^{18,19} Further information on the fitting procedure is given in the Supporting Information.

$$H = \sum_{i=1}^4 Bg_i S_i + \sum_{i=1}^4 S_i D S_i + \sum_{i=1, j=2, i \neq j}^4 S_i J_{ij} S_j$$

Electrochemistry. Cyclic voltammograms (CVs) were measured by using a 0.2-mm-diameter glassy-carbon or platinum-disk working electrode, a platinum auxiliary electrode, and a silver-wire pseudoreference or a Ag/AgNO_3 (0.10 M in MeCN) reference electrode. Measurements were performed at room temperature using a PAR 263 potentiostat. All electrochemical measurements were performed in CH_2Cl_2 or MeCN in an Mbraun glovebox under a dinitrogen atmosphere. The redox potentials of 2 mM concentrations of the samples were measured in the presence of 0.50 M $^n\text{Bu}_4\text{N}(\text{PF}_6)$, using $[\text{Fe}(\eta^5\text{-C}_5\text{H}_5)_2]^{+/0}$ ($\text{Cp}_2\text{Fe}^+/\text{Cp}_2\text{Fe}$) as internal standard ($\Delta E_p = 80$ mV at 100 mV s^{-1}). All redox potentials are quoted relative to $\text{Cp}_2\text{Fe}^+/\text{Cp}_2\text{Fe}$.

Results and Discussion

Synthesis and Optical Spectroscopic Characterization: Conversion between Tetra-, Tri-, Di-, and Monoiron(II) Complexes. The synthetic routes for the preparation of complexes 1–12 and their interconversion are depicted in Scheme 1. Complex 1 was prepared via self-assembly by reacting $\text{Fe}(\text{OTf})_2 \cdot 2\text{MeCN}$ with NaO_2Cbiph in a 1:2 ratio in THF. Warming the powdered tetranuclear complex 1 in a mixture of MeCN/ CH_2Cl_2 allowed the linear trinuclear iron(II) complex 6 to be obtained in 83% yield. The two medium-intensity absorptions at 2304 and 2276 cm^{-1} in the IR spectrum of 6 are assigned as the symmetric and asymmetric combination $\text{C}\equiv\text{N}$ stretching bands for the two

(14) Kent, T. A. *WMOSS: Mössbauer Spectral Analysis Software*, version 2.5; WEB Research Co.: Minneapolis, MN, 1998.

(15) Drago, R. S. *Physical Methods for Chemists*, 2nd ed.; Saunders: Orlando, FL, 1992.

(16) Krzystek, J.; Park, J.-H.; Meisel, M. W.; Hitchman, M. A.; Stratemeier, H.; Brunel, L.-C.; Telser, J. *Inorg. Chem.* **2002**, *41*, 4478–4487.

(17) Goldberg, D. P.; Telser, J.; Bastos, C. M.; Lippard, S. J. *Inorg. Chem.* **1995**, *34*, 3011–3024.

(18) Abragam, A.; Bleaney, B. *Electron Paramagnetic Resonance of Transition Ions*; Dover Publications, Inc.: New York, 1986.

(19) Boča, R. *Coord. Chem. Rev.* **2004**, *248*, 757–815.

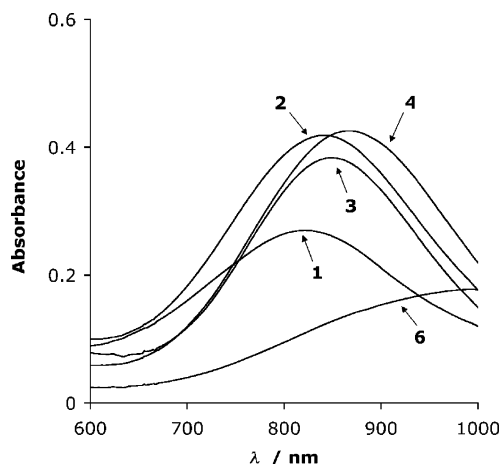


Figure 2. Electronic absorption spectra of **1–4** measured 2 min after the addition of the azole ligands (**2–4**) or THF (**1**) to a 6 mM solution of **6** in CH_2Cl_2 . The UV–vis spectrum of **6** is also shown.

acetonitrile ligands per terminal iron atom, as observed in the X-ray crystal structure of **6** (see below).

Reactions of **6** for several minutes in THF or in a mixture of dimethoxyethane/acetonitrile/dichloromethane with heating resulted in ligand displacement to afford **7** or **8**, respectively, with preservation of the overall triiron(II) composition. Yellow blocks were isolated upon crystallization of the trinuclear product in 69 and 67% yield for **7** and **8**, respectively. Stirring complex **6** in THF at room temperature gave a pale-green solution, indicative of the formation of a tetranuclear species. Upon concentration to dryness, complex **1** crystallized from a green CH_2Cl_2 solution with pentane vapor diffusion as pale-green blocks in 80% yield, demonstrating the reversible interconversion of **1** and **6**. However, the initial crystallization of **1** produced a yellow supernatant, which upon further recrystallization from the same solvent mixture gave yellow crystals of **7** in small yield (~10%). This result indicates that the trinuclear species forms as a minor byproduct that is more soluble than the tetranuclear species **1**.

The tetrairon(II) complexes $[\text{Fe}_4(\text{O}_2\text{Cbiph})_8(\text{L})_2]$ (**2–5**) were isolated by reacting **6** with 2 equiv (with respect to the products) of the weak azole ligands (N_{weak}) indazole (Hind), pyrazole (Hpz), and 3,5-dimethylpyrazole (Hdimepz) and acetamide. In these reactions, the color of the reaction mixture changed from yellow to pale green. The formation of complexes **1–4** was followed by electronic spectroscopy; we monitored the appearance of broad absorption bands at 824 (50), 836 (70), 847 (65), and 862 nm ($\epsilon \sim 70 \text{ M}^{-1} \text{ cm}^{-1}$), respectively (Figure 2). The significantly smaller intensity for the absorption in **1** might be explained by the formation of **7** as a minor byproduct; **7** has no absorption band in the low-energy region of the UV–vis spectrum. For all complexes, no further spectral changes were observed after 2 min. Compounds **1–4** also display high-intensity absorption bands in the UV region ($\lambda < 350 \text{ nm}$) originating from the 2-biphenylcarboxylate ligands. Pale-green crystals were isolated in all cases from CH_2Cl_2 and pentane vapor diffusion in 69, 80, 66, and 51% yield for **2–5**, respectively. For **2–5**, no complexes with different nuclearity could be isolated,

even when reacting 4–6 equiv (with respect to the products) of the donors with **6** in CH_2Cl_2 . The N–H stretching frequencies at 3401, 3367, 3342, and 3478 cm^{-1} for **2–5**, respectively, confirm the presence of the coordinated and protonated heterocycles or acetamide ligand in the complexes. Strong ν_{asym} carboxylate absorption bands from the $^-\text{O}_2\text{Cbiph}$ ligand dominate the IR spectrum of **5**, obscuring the carbonyl stretch of acetamide.

The paddlewheel complexes $[\text{Fe}_2(\text{O}_2\text{Cbiph})_4(\text{L})_2]$ (**9** and **10**) were prepared by reacting 2–3 equiv (with respect to the products) of the strong N-donors (N_{strong}) pyridine (py) or 1-methylimidazole (1-MeIm) with **1** or **6** in CH_2Cl_2 . Yellow blocks were isolated in 86 and 88% yields, respectively. Following the reaction by UV–vis spectroscopy indicated the conversion to be complete within 2 min. A low-energy band at 843 ($\epsilon \sim 60 \text{ M}^{-1} \text{ cm}^{-1}$) or 912 nm ($\epsilon \sim 70 \text{ M}^{-1} \text{ cm}^{-1}$) for **9** and **10**, respectively, appeared during the reaction. Red-shifted bands that move to lower energy with increasing donor strengths of the axial ligands were previously reported for paddlewheel dirhodium(II) acetate complexes.²⁰ Although reactions of **1** or **6** in neat py under similar experimental conditions gave compound **9** in high yield (84%), reacting **1**, **6**, or **10** with excess or neat 1-MeIm resulted in only some crystals of the mononuclear species $[\text{FeCl}_2(1\text{-MeIm})_4]$ (**11**). In this complex, the X-ray structure of which is given in the Supporting Information, the chloro ligands most likely originate from chlorine abstraction from the solvent CH_2Cl_2 . A homoleptic octahedral 1-methylimidazolemonoiron complex (**12**) was also identified by X-ray crystallography, but the structure was not good enough for us to assign the counterions in the lattice. These results indicate that a large excess of 1-MeIm should be avoided in the synthesis of **10**. The reaction of 2.2 equiv of 1-MeIm with $[\text{Fe}_2(\mu\text{-O}_2\text{CAr}^{\text{Tol}})_2(\text{O}_2\text{CAr}^{\text{Tol}})_2(\text{THF})_2]$ resulted in the formation of $[\text{Fe}_2(\mu\text{-O}_2\text{CAr}^{\text{Tol}})_2(\text{O}_2\text{CAr}^{\text{Tol}})_2(1\text{-MeIm})_2]$,²¹ and the addition of 1-MeIm to $[(\text{Mes}_2\text{ArCO}_2)_2\text{Li}(\text{Et}_2\text{O})]_2$ and FeCl_2 or $\text{Fe}(\text{OTf})_2$ in CH_2Cl_2 gave the mononuclear complex $[(\text{Mes}_2\text{ArCO}_2)_2\text{Fe}(1\text{-MeIm})_2]$ as colorless crystals, irrespective of the amount of 1-MeIm used in the reaction (1 equiv to a large excess).²²

The $\text{p}K_{\text{a}}$ values for protonation at the metal-binding sites of the heterocycles (azole/azolium couple) are 1.25, 2.48, 4.06, 5.30, and 7.12 for Hind, Hpz, Hdimepz, py, and 1-MeIm, respectively (Table 3).²³ The $\text{p}K_{\text{a}}$ value is a measure of the σ -donor strength for a given ligand and correlates with the net electron-donor properties, expressed by the ligand electrochemical parameter E_{L} , for a series of azole ligands.²⁴ E_{L} parameters were also reported to correlate with Hammett substituent parameters (σ).²⁵ These parameters allow the three

(20) Johnson, S. A.; Hunt, H. R.; Neumann, H. M. *Inorg. Chem.* **1963**, *2*, 960–962.

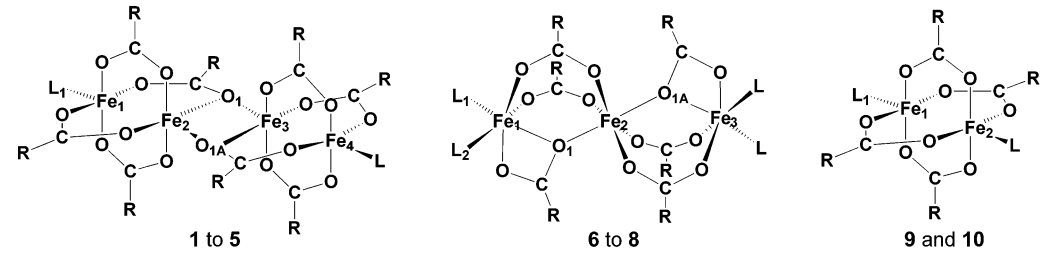
(21) Lee, D.; Lippard, S. J. *J. Am. Chem. Soc.* **1998**, *120*, 12153–12154.

(22) Hagadorn, J. R.; Que, L., Jr.; Tolman, W. B. *J. Am. Chem. Soc.* **1998**, *120*, 13531–13532.

(23) Catalan, J.; Abboud, J. L. M.; Elguero, J. *Adv. Heterocycl. Chem.* **1987**, *41*, 187–274.

(24) Reisner, E.; Arion, V. B.; Eichinger, A.; Kandler, N.; Giester, G.; Pombeiro, A. J. L.; Keppler, B. K. *Inorg. Chem.* **2005**, *44*, 6704–6716.

(25) Masui, H.; Lever, A. B. P. *Inorg. Chem.* **1993**, *32*, 2199–2201.

Table 3. Selected Bond Distances (Å) and Angles (deg) for Complexes 1–10


	[Fe _n (O ₂ Cbiph) _{2n} (L) _m]									
	Cpd	n	m	L						
	1	4	2	THF						
	2	4	2	Hind						
	3	4	2	Hpz						
	4	4	2	Hdimepz						
	5	4	2	acetamide						
	6	3	4	MeCN						
	7	3	4	THF						
	8	3	2	DME						
	9	2	2	py						
	10	2	2	1-Melm						

	1	2·2CH ₂ Cl ₂	3	4a·4CH ₂ Cl ₂	5·2C ₆ H ₅ Cl	6a	7	8	9·CH ₂ Cl ₂	10·CH ₂ Cl ₂
	Atom1–Atom2 (Å)									
Fe(1)–Fe(2)	2.8360(5)	2.8239(5)	2.8506(12)	2.878[3]	2.8656(7)	3.5790(6)	3.565 [22]	3.606(3)	2.8912(7)	2.9348(13)
Fe(2)–Fe(3)	3.4658(6)	3.4266(7)	3.4579(15)	3.402[13]	3.4569(9)					
Fe(1)–L(1)	2.0694(12)	2.061(2)	2.051(3)	2.068[6]	2.040(2)	2.1388(18)	2.110[15]	2.264(2)	2.1181(12)	2.0947(18)
Fe(1)–L(2)						2.246(2)	2.205[19]	2.131(2)		
Fe(2)–O(1,syn)	2.1997(12)	2.2131(16)	2.196(2)	2.229[1]	2.2783(19)					
Fe(2)–O(1A,anti)	2.0841(12)	2.0845(16)	2.082(2)	2.075[1]	2.0775(18)					
Fe–O _{min}	1.9973(13)	2.0012(16)	1.993(2)	1.999(1)	1.9964(18)	1.9856(14)	2.0114(14)	1.989(2)	2.0467(11)	2.0381(16)
Fe–O _{max}	2.1997(12)	2.2131(16)	2.196(2)	2.229(1)	2.2783(19)	2.2915(14)	2.2847(14)	2.2637(18)	2.0938(11)	2.1609(15)
Fe(1)–O _{mean} obs ^a	2.081[8] ^c	2.071[27]	2.066[17]	2.082[21]	2.080[5]	2.121[63]	2.126[34]	2.115[56]	2.062[11]	2.076[29]
Fe(1)–O _{mean} calcd ^b	2.073	2.097	2.101	2.095	2.073	2.163	2.140	2.140	2.080	2.087
Fe(2)–O _{mean} obs ^a	2.070[36]	2.076[37]	2.071[35]	2.080[28]	2.082[51]	2.114[35]	2.119[28]	2.129[12]		
Fe(2)–O _{mean} calcd ^b	2.073	2.073	2.073	2.073	2.073	2.140	2.140	2.140		
	Atom1–Atom2–Atom3 (deg)									
Fe(1)–Fe(2)–Fe(3)	112.45(1)	112.09(2)	113.46(3)	111.9(4)	108.95(2)	180	175.82(1)	180		
Fe(2)–O(1)–Fe(3/1)	107.97(5)	105.71(7)	107.84(9)	104.4(6)	104.96(7)	106.99(6)	105.9[22]	110.93(8)		
Fe(1)–Fe(2)–O(1)	77.64(3)	76.76(4)	78.57(5)	76.0(7)	73.62(4)	37.76(4)	37.7[11]	35.17(5)		
Fe(1)–Fe(2)–O(1A)	149.42(4)	149.48(5)	150.49(6)	150.6(1)	148.16(5)	142.24(4)	142.5[14]	144.83(5)		
Fe(2)–Fe(1)–L(1)	166.35(4)	166.24(6)	166.90(7)	162.4(7)	158.67(6)	158.26(5)	161.81[6]	155.53(4)	164.29(3)	161.05(4)
Fe(2)–Fe(1)–L(2)						111.97(5)	102.5[18]	130.47(4)		
τ ₁ , ^c Fe(1)	0.16	0.09	0.32	0.26	0.02				0.01	0.02
τ ₂ , ^c Fe(2)	0.15	0.07	0.27	0.23	0.02					
pK _a (N-heterocycle) ^d		1.25	2.48	4.06					5.30	7.12

^a The observed unweighted mean value and its standard deviation for Fe–O(carboxylate) are given.²⁶ ^b Calculated Fe–O distances based on bond valence sum analysis (see the Supporting Information). ^c $\tau = (\beta - \alpha)/60$, where β and α are the largest and second largest bond angles, respectively. For a perfectly square-pyramidal geometry, τ is zero, and it becomes unity for a perfectly trigonal-bipyramidal geometry. Addison, A. W.; Rao, T. N.; Reedijk, J.; van Rijn, J.; Verschoor, G. C. *J. Chem. Soc., Dalton Trans.* **1984**, 1349–1356. ^d Taken from ref 23. ^e See ref 26.

sets of N donors used in this study to be distinguished. The weak N donors (Hind, Hpz, and Hdimepz) are not capable of breaking the doubly single-atom bridged {Fe₂O₂} center, and the tetranuclear paddlewheel association therefore remains intact in complexes 2–4. Strong N donors (py and 1-Melm) break the *dimer of dimers* structure within several minutes, affording the yellow paddlewheel dimers 9 and 10. When a large excess of the very strong N-donor 1-Melm is used, all 2-biphenylcarboxylate ligands are replaced and only mononuclear species 11 and 12 are isolated.

Complexes 1–10 are very sensitive to air, and both dichloromethane solutions and the crystalline material turn brown within seconds or minutes when exposed to the atmosphere. Complex 9 shows an absorption band at 382 nm ($\epsilon_{\max} = 2100 \text{ M}^{-1} \text{ cm}^{-1}$) in CH₂Cl₂, and the corresponding spectral changes were followed by UV–vis spectroscopy after bubbling dry dioxygen through a solution of the compound at $-78 \text{ }^\circ\text{C}$. This oxygenation produces a metastable derivative of 9, as indicated by the appearance of a new band in the visible spectrum, at 477 nm ($\epsilon_{\max} = 1200 \text{ M}^{-1} \text{ cm}^{-1}$), which starts to decay after several hours (see the Supporting Information). Although crystalline blocks of 6 are stable under a dinitrogen atmosphere for several weeks at room temperature, pulverizing the sample or drying it under high vacuum results in decomposition within several

days, as indicated by a color change to brown. Elemental analyses after drying a sample of 6 under high vacuum indicate a loss of all acetonitrile ligands (% N \approx 0).

Structural Characterization. The *dimer of dimers* structures of 1 and 4 are depicted in Figures 3 and 4, and Table 3 lists selected bond lengths and angles for 1–5. All molecules except 4b have a crystallographically required center of symmetry, and the four metal atoms lie in one geometric plane with a dihedral angle of $\Theta_{\text{Fe}(1)\text{--Fe}(2)\text{--Fe}(2A)\text{--Fe}(1A)} = 180^\circ$ as required by symmetry. The {Fe₂(O₂Cbiph)₄}₂ core is held together by two μ_2 -1,1 bridges from the *syn,syn,anti- μ_3 -3,1,1*-biphenylcarboxylate ligands. As expected, the 2.851–[10]²⁶ Å Fe(1)–Fe(2) (quadruply bridged) distances are considerably shorter than the 3.442[12] Å Fe(2)–Fe(2A) (doubly bridged) distances, and the mean Fe^{II}–O(carboxylate) bond lengths fall in the expected range between 1.993(2) and 2.2783(19) Å in 1–5. The axial pockets generated by four bridging 2-biphenylcarboxylates circumscribe the apical positions of the exogenous ligands in 1–5. The Fe–O bond distance to the terminally bound THF molecule in 1 is slightly shorter than the Fe–O(THF) bond

(26) Parentheses refer to unique values and square brackets to average values calculated by the following equations. Considering a sample of n observations x_i , the unweighted mean value (x_u) with its standard deviation (σ) was calculated using the following equations: $x_u = \sum x_i/n$ and $\sigma = \{[\sum (x_i - x_u)^2 / (n - 1)]^{1/2}$.

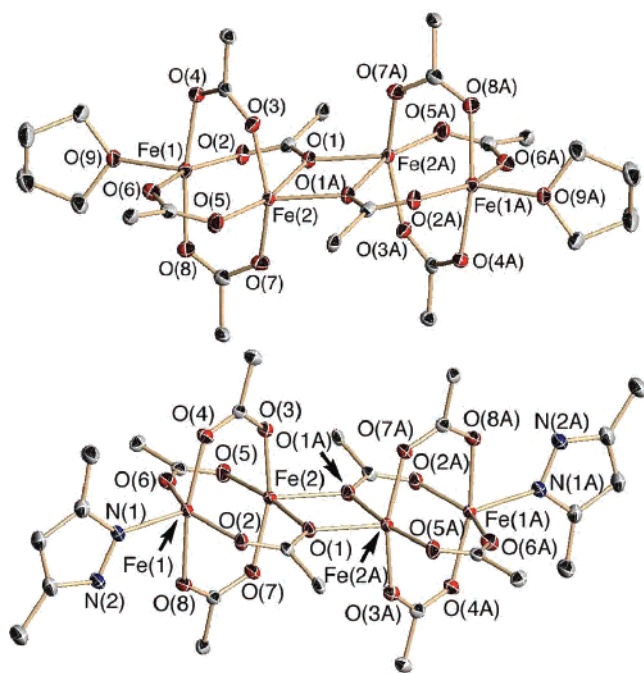


Figure 3. ORTEP diagram of **1** (top) and **4a** (bottom) showing 50% probability thermal ellipsoids for all non-hydrogen atoms. The solvent molecules of **4a** and the aromatic rings of the $^{-}\text{O}_2\text{C}$ biph ligands (except the α -carbon atom) for both compounds were omitted for clarity.

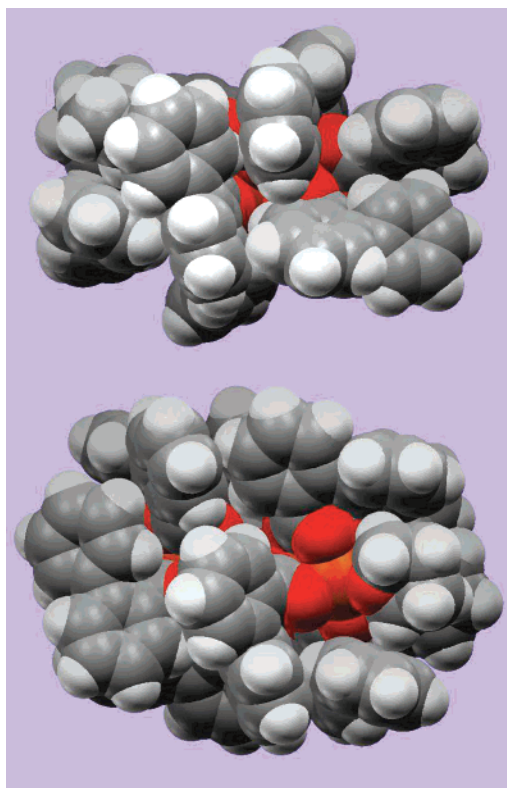


Figure 4. Space-filling view of **1** along the b axis (top) and orientated parallel to the ac plane showing the disposed Fe^{II} center (bottom).

lengths of 2.0941(19) Å in $[\text{Fe}_2(\mu\text{-O}_2\text{C}^{\text{Tot}})_2(\text{O}_2\text{C}^{\text{Tot}})_2(\text{THF})_2] \cdot 2\text{CH}_2\text{Cl}_2$.²¹ The $\text{Fe}^{\text{II}}\text{-N}$ bond distances in **2–4** are comparable with values previously reported for carboxylate-rich iron compounds.^{21,22,27}

(27) Lee, D.; Lippard, S. J. *Inorg. Chem.* **2002**, *41*, 2704–2719.

The X-ray crystal structure of **5** reveals infinite chains of molecules held together by an intermolecular acetamide hydrogen-bonding network along the a axis having $\text{N}(1)\text{-O}(9\text{B}) = 2.9773(34)$ Å and $\text{N}(1)\text{-O}(4\text{B}) = 2.8951(32)$ Å (Figure S6 in the Supporting Information). The hydrogen bonding between two amide ligands consists of an eight-membered $\text{N}(1)\text{-H}(2\text{N})\cdots\text{O}(9\text{B})\text{-C}(1\text{B})\text{-N}(1\text{B})\text{-H}(2\text{NB})\cdots\text{O}(9)\text{-C}(1)$ ring. The respective $\text{O}(9)=\text{C}(1)$ and $\text{C}(1)\text{-N}(1)$ bond lengths of 1.248(3) and 1.312(4) Å are consistent with reported distances for the acetamide tautomer found in an allenedicarboxylic acid/acetamide complex, where $\text{C}=\text{O}$ and $\text{N}\text{-C}$ are 1.251(2) and 1.316(3) Å, respectively.²⁸ The coordination via O(9) instead of the acetamide nitrogen atom or its imine tautomer can be rationalized as a consequence of the stabilizing influence of the strong hydrogen-bonding network involving the amide ligand, which would be compromised by N donation to iron. The $\text{Fe}(1)\text{-O}(\text{amide})$ bond distance of 2.040(2) Å is significantly longer than that in a dithiocarbamate complex $[\text{Fe}(\text{OC}_4\text{H}_8\text{dtc})_2(\text{DMF})]$, where $\text{Fe}^{\text{II}}\text{-O}(\text{DMF})$ is 1.983(7) Å.²⁹ The $\text{N}\text{-H}$ stretching frequency at 3478 cm^{-1} confirms the presence of the amide. To the best of our knowledge, **5** is the first structurally characterized iron(II) complex containing a coordinated acetamide.

A closer examination of compounds **1–5** reveals that the asymmetric 2-phenylbenzoate ligand facilitates a tetranuclear arrangement. In these compounds, the phenyl rings in ortho positions of the benzoate groups are oriented outward, away from the linked paddlewheel subunits, preventing further self-association through the anti lone pairs of the bridging carboxylate oxygen atoms and allowing for the isolation of discrete tetranuclear complexes. None of the 2-biphenylcarboxylate ligands in complexes **1–5** points toward the center of the molecule (Figure 4 and the Supporting Information). More sterically hindered symmetric terphenyl-based carboxylates shield both sides of the diiron core, preventing association of the dinuclear subunits into tetranuclear species. A large number of publications describe tetranuclear iron–sulfur³¹ and organometallic clusters, but only a relatively small number of compounds have been reported that contain carboxylate-bridged tetranuclear iron clusters, despite the importance of iron–oxo clusters in bioinorganic chemistry. The reported $\{\text{Fe}_4\}$ cores can be roughly categorized into four structural types: adamantane $\{\text{Fe}_4\text{O}_6\}$ cores,³² face-to-face $\{\text{Fe}_4\text{O}_6\}$ cores,³³ cubane $\{\text{Fe}_4\text{O}_4\}$ cores,³⁴ and butterfly

(28) Berkovitch-Yellin, Z.; Leiserowitz, L.; Nader, F. *Acta Crystallogr., Sect. B: Struct. Sci.* **1977**, *B33*, 3670–3677.

(29) Deng, Y.; Wen, T.; Liu, Q.; Zhu, H.; Chen, C.; Wu, D. *Inorg. Chim. Acta* **1999**, *293*, 95–99.

(30) *ConQuest*, version 1.8; Cambridge Crystallographic Data Center: Cambridge, U.K., 2006.

(31) Rao, V. P.; Holm, R. H. *Chem. Rev.* **2004**, *104*, 527–559.

(32) (a) Murch, B. P.; Boyle, P. D.; Que, L., Jr. *J. Am. Chem. Soc.* **1985**, *107*, 6728–6729. (b) Murch, B. P.; Bradley, F. C.; Boyle, P. D.; Papaefthymiou, V.; Que, L., Jr. *J. Am. Chem. Soc.* **1987**, *109*, 7993–8003. (c) Drüeke, S.; Wieghardt, K.; Nuber, B.; Weiss, J.; Bominaar, E. L.; Sawaryn, A.; Winkler, H.; Trautwein, A. X. *Inorg. Chem.* **1989**, *28*, 4477–4483. (d) Sessler, J. L.; Sibert, J. W.; Burrell, A. K.; Lynch, V.; Markert, J. T.; Wooten, C. L. *Inorg. Chem.* **1993**, *32*, 4277–4283.

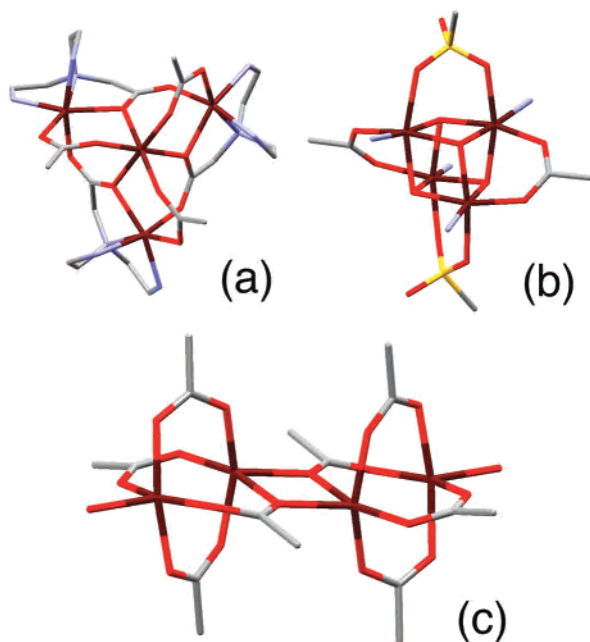
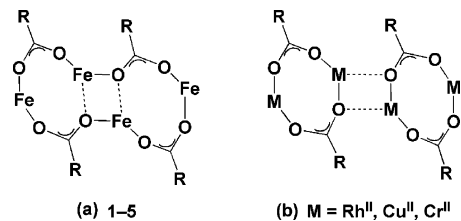


Figure 5. Capped-sticks core representations of tetranuclear ferrous complexes containing carboxylate bridging ligands with three distinct geometries: (a) $[\text{Fe}_4^{\text{II}}(\text{bpg})_3(\text{O}_2\text{CPh})_3](\text{ClO}_4)_2$ with an iron atom sitting on a C_3 -symmetry axis; (b) cubane core of $[\text{Fe}_4^{\text{II}}(\mu\text{-OH})_4(\mu\text{-O}_2\text{CAR}^{4\text{-tBuPh}})_2(\mu\text{-OTf})_2(4\text{-tBupy})_4]$; (c) planar carboxylate-bridged tetrairon(II) cluster **1**. Color code: Fe, dark red; O, red; C, gray; N, blue; S, yellow.

$\{\text{Fe}_4\text{O}_2\}$ cores.³⁵ Although most of these complexes contain mainly ferric ions, some tetranuclear ferrous complexes with bridging carboxylate ligands have also been described. A tetrairon(II) aggregate $[\text{Fe}_4^{\text{II}}(\text{bpg})_3(\text{O}_2\text{CPh})_3](\text{ClO}_4)_2$ with three identical $\{\text{Fe}(\text{bpg})(\text{O}_2\text{CPh})\}$ units coordinated to a central Fe^{II} ion displaying threefold symmetry and an $\text{Fe}\text{--}\text{Fe}(\text{center})$ distance of 3.393(7) Å has been synthesized (Figure 5a).³⁶ Cubane-type Fe^{II}_4 clusters have been isolated and crystallographically characterized.³⁷ $[\text{Fe}_4(\mu\text{-OH})_4(\mu\text{-O}_2\text{CAR}^{4\text{-tBuPh}})_2(\mu\text{-OTf})_2(4\text{-tBupy})_4]$ ($^-\text{O}_2\text{CAR}^{4\text{-tBuPh}} = 2,6\text{-bis}(4\text{-tert-butylphenyl})\text{benzoate}$) with a $\{\text{Fe}_4(\mu\text{-OH})_4\}^{4+}$ core is depicted in Figure 5b. The $\text{Fe}^{\text{II}}\text{--}\text{Fe}^{\text{II}}$ distances in this tetrairon cube vary between 3.0605(8) and 3.2508(8) Å.³⁸ Iron paddlewheel associations with a $\{\text{Fe}_4(\mu\text{-O}_2\text{CR})_8\}$ core (**1–5**; Figures 1, 3, and 5c) have not been previously reported.³⁰

The association of paddlewheel dimers into polymers is known,³⁹ and the isolation and structural characterization of

Chart 3



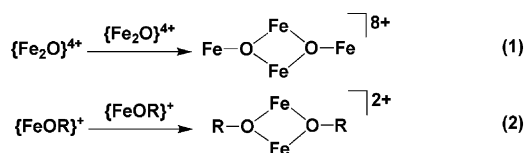
discrete *dimer of dimers* structures has been reported for rhodium(II),⁴⁰ copper(II),⁴¹ and chromium(II)⁴² complexes. In all previously studied compounds, the association via the monoatom-bridging oxygen is usually weak, with $\text{M}\text{--}\text{O}_{\text{anti}}$ distances between 2.22 and 2.61 Å.^{41,43} This result is in agreement with the generally accepted higher basicity of syn rather than anti lone pairs in carboxylate ligands.⁴⁴ Examples with $\text{M}\text{--}\text{O}_{\text{syn}}$ longer than the $\text{M}\text{--}\text{O}_{\text{anti}}$ distances are not known for homometallic carboxylate-bridged *dimer of dimers* constructs. Complexes **1–5** feature a strong self-association, with coordinative covalent bonds displaying mean $\text{Fe}(2)\text{--}\text{O}(1\text{A})$ bond distances (anti coordination) of 2.081[2] Å, compared to the considerably longer $\text{Fe}(2)\text{--}\text{O}(1)$ bond lengths of 2.223[15] Å (Chart 3) for the syn binding mode. The strong interaction between the two $\{\text{Fe}_2(\text{O}_2\text{CR})_4\}$ dimers explains the unchanged tetranuclear arrangement in complexes **2–5** even when azole (N_{weak}) and acetamide are used as the exogenous ligands. The donor properties of azole and acetamide are weaker than the strong dimeric interaction, and therefore they serve only as exogenous terminal ligands in the tetranuclear compounds, replacing the weaker THF ligands in **1**. All *dimer of dimers* structures reported so far in the literature have only either very weak (e.g., THF) or no exogenous ligands. The dimer–dimer interactions in these molecules are weak, as indicated by long $\text{Fe}\text{--}\text{O}_{\text{anti}}$ bond lengths (see above).⁴⁵ Use of a stronger exogenous ligand would probably break these weak dimer–dimer interactions, preventing their isolation as tetranuclear species. Only *dimer of dimers* complexes with strong interdimer interactions, as found in **2–4**, can accommodate relatively strong exogenous ligands such as azoles, preventing them from disrupting the association of paddlewheels.

Examples of iron carboxylate polymers include $[\text{Fe}^{\text{II}}(\mu\text{-CF}_3\text{CO}_2)_2(\text{CF}_3\text{CO}_2\text{H})_2]_n$, which has bridging trifluoroacetate

- (33) (a) Jameson, D. L.; Xie, C.-L.; Hendrickson, D. N.; Potenza, J. A.; Schugar, H. J. *J. Am. Chem. Soc.* **1987**, *109*, 740–746. (b) Satcher, J. H., Jr.; Olmstead, M. M.; Droegge, M. W.; Parkin, S. R.; Noll, B. C.; May, L.; Balch, A. L. *Inorg. Chem.* **1998**, *37*, 6751–6758. (c) Chen, Q.; Lynch, J. B.; Gomez-Romero, P.; Ben-Hussein, A.; Jameson, G. B.; O'Connor, C. J.; Que, L., Jr. *Inorg. Chem.* **1988**, *27*, 2673–2681.
- (34) Taft, K. L.; Caneschi, A.; Pence, L. E.; Delfs, C. D.; Papaefthymiou, G. C.; Lippard, S. J. *J. Am. Chem. Soc.* **1993**, *115*, 11753–11766.
- (35) Armstrong, W. H.; Roth, M. E.; Lippard, S. J. *J. Am. Chem. Soc.* **1987**, *109*, 6318–6326.
- (36) Ménage, S.; Fujii, H.; Hendrich, M. P.; Que, L., Jr. *Angew. Chem., Int. Ed.* **1994**, *33*, 1660–1662.
- (37) (a) Clemente-Juan, J. M.; Mackiewicz, C.; Verelst, M.; Dahan, F.; Bousseksou, A.; Sanakis, Y.; Tuchagues, J.-P. *Inorg. Chem.* **2002**, *41*, 1478–1491. (b) Oshio, H.; Hoshino, N.; Ito, T.; Nakano, M. *J. Am. Chem. Soc.* **2004**, *126*, 8805–8812.
- (38) Lee, D.; Sorace, L.; Caneschi, A.; Lippard, S. J. *Inorg. Chem.* **2001**, *40*, 6774–6781.

- (39) (a) Drew, M. G. B.; Edwards, D. A.; Richards, R. *Chem. Commun.* **1973**, 124–125. (b) Bird, M. J.; Lomer, T. R. *Acta Crystallogr., Sect. B: Struct. Sci.* **1972**, *B28*, 242–246. (c) Mounts, R. D.; Ogura, T.; Fernando, Q. *Inorg. Chem.* **1974**, *13*, 802–805.
- (40) (a) Cotton, F. A.; Hillard, E. A.; Liu, C. Y.; Murillo, C. A.; Wang, W.; Wang, X. *Inorg. Chim. Acta* **2002**, *337*, 233–246. (b) Cotton, F. A.; Dikarev, E. V.; Stiriba, S.-E. *Inorg. Chem.* **1999**, *38*, 4877–4881. (c) Dikarev, E. V.; Andreini, K. W.; Petrukina, M. A. *Inorg. Chem.* **2004**, *43*, 3219–3224. (d) Alarcón, C. J.; Lahuerta, P.; Peris, E.; Ubeda, M. A.; Aguirre, A.; García-Granda, S.; Gómez-Beltrán, F. *Inorg. Chim. Acta* **1997**, *254*, 177–181.
- (41) Kozlevčar, B.; Leban, I.; Petrič, M.; Petriček, S.; Roubeau, O.; Reedijk, J.; Šegedin, P. *Inorg. Chim. Acta* **2004**, *357*, 4220–4230.
- (42) Cotton, F. A.; Thompson, J. L. *Inorg. Chem.* **1981**, *20*, 3887–3890.
- (43) Chisholm, M. H.; Folting, K.; Moodley, K. G.; Wesemann, J. E. *Polyhedron* **1996**, *15*, 1903–1905.
- (44) Carrell, C. J.; Carrell, H. L.; Erlebacher, J.; Glusker, J. P. *J. Am. Chem. Soc.* **1988**, *110*, 8651–8656.
- (45) Cotton, F. A.; Thompson, J. L. *Inorg. Chem.* **1981**, *20*, 1292–1296.

ligands arranged in a windmill configuration,⁴⁶ and a mixture of μ_3 -syn,syn,anti- and μ_2 -syn,syn-bridging carboxylates in $[\text{Fe}^{\text{II}}(\text{O}_2\text{CH})_2\text{-}^{1/3}\text{HCO}_2\text{H}]_n$,⁴⁷ $[\text{Fe}^{\text{II}}_3(\mu\text{-O}_2\text{CMe})_6(\kappa\text{-O-DMSO-d}_6)_2]_n$,⁴⁸ and $[\text{Fe}^{\text{II}}_2(\mu\text{-O}_2\text{CMe})_4(\text{py})_3]_n$.⁴⁸ In addition, oxalate ligands form iron(II) polymers with μ_2 -anti,anti-⁴⁹ and μ_3 -syn,anti,anti-binding^{49,50} modes. Tetrairon complexes often result from the formal dimerization of two diiron cores, as we previously observed in the oxo-bridged tetrairon(III) complexes $(\text{Et}_4\text{N})[\text{Fe}^{\text{III}}_4\text{O}_2(\text{O}_2\text{CR})_7(\text{H}_2\text{B}(\text{pz})_2)_2]$,³⁵ where $\text{R} = \text{Me}$ or Ph and $\text{H}_2\text{B}(\text{pz})_2^- =$ dihydrobis(1-pyrazolyl)borate, and in $[\text{Fe}^{\text{III}}_4\text{O}_2(\text{BICOH})_2(\text{BICO})_2(\text{O}_2\text{CPh})_4]\text{Cl}_2$, where $\text{BICOH} =$ bis(*N*-methylimidazol-2-yl)carbinol.⁵¹ The ferric complexes were formulated as the 2 + 2 condensation products of two $\{\text{Fe}^{\text{III}}_2\text{O}\}^{4+}$ cores, resulting in $\{\text{Fe}^{\text{III}}_4\text{O}_2\}^{8+}$ associations (eq 1). The related dimerization of two $\{\text{Fe}(\text{O}_2\text{CR})\}^+$ cores in **1–5** is shown in eq 2.



The carboxylate ion has one delocalized negative charge, and each sp^2 oxygen atom has two lone pairs disposed at an angle of 120° with respect to each other. The syn-coordination mode is more frequently observed⁵² and has a higher Lewis basicity than binding through the anti lone pair.⁵³ Although a preference for syn coordination of metal ions to carboxylate ligands has been noted in a survey of the Cambridge Structural Database, a syn preference for the carboxylate ligand is not demonstrated by all metal ions.⁴⁴ For all metal complexes evaluated, the distribution is 63% syn, 23% anti, and 14% *direct* binding (i.e., bidentate coordination to a single metal center). From a large number of transition metals, only Fe^{II} , Mn^{III} , Co^{III} , and Pt^{II} preferably adopt the anti-coordination mode.⁴⁴ This empirical survey explains the unprecedented shorter $\text{M}-\text{O}_{\text{anti}}$ than $\text{M}-\text{O}_{\text{syn}}$ bond distances and the strong dimer interaction in the paddlewheel associations within **1–5**. In addition, it shows the importance of steric shielding around the carboxylate center whether in model compounds or in a protein environment for diiron(II) systems. Both iron(III), and presumably iron(IV), have a large preference for syn coordination,⁴⁴ and

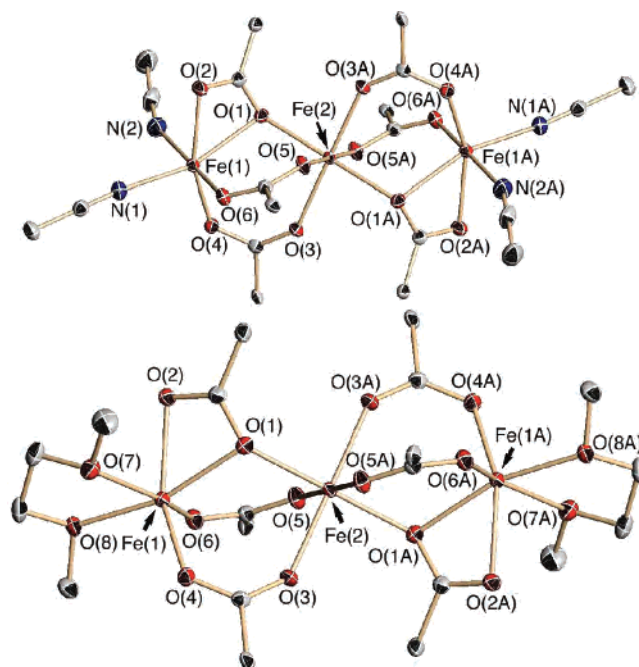


Figure 6. ORTEP diagrams of **6a** (top) and **8** (bottom) showing 50% probability thermal ellipsoids for all non-hydrogen atoms. All atoms of the O_2Cbiph ligands, except for the carboxylate group and the α -carbon atom, were omitted for clarity.

the enforced syn-coordination mode of the carboxylate ligands to the Fe^{II} ions in MMOH_{red} might help to store energy to reach the active diiron(IV) intermediate **Q** in the catalytic cycle of MMOH , which is ultimately responsible for the conversion of methane to methanol. Syn coordination might act as an energy reservoir to destabilize the low-valent intermediate. The compression of the Fe^{II}_2 core, possibly by the positioning of the γ subunit in MMOH_{red} ($\text{Fe}-\text{Fe} \sim 3.3 \text{ \AA}$),⁵⁴ was recently revealed by computational studies. This work demonstrated how the protein matrix can affect the active site geometry, destabilizing intermediates that lie closer in energy to reduced forms of the enzyme and facilitating the formation of the methane-oxidizing diiron(IV) species **Q**.⁵⁵

The solid-state structures of **6** and **8** are depicted in Figure 6. Selected bond lengths and angles are given in Table 3. The central atom in **6** and **8** is located on a crystallographic inversion center, resulting in a symmetry-required linear disposition of iron atoms. The corresponding angle in **7** is $175.82(1)^\circ$, giving a slightly bent array of iron atoms. The compositions of **6–8** involve three Fe^{II} ions; six bidentate carboxylate ligands bridge two iron atoms flanking the central atom. Four biphenylcarboxylate ligands bridge in the common μ_2 -syn,syn mode and two link the three iron atoms in a syn,syn,anti- μ_3 -3,1,1 configuration, completing the octahedral coordination sphere at $\text{Fe}(2)$. The termini of the $\{\text{Fe}^{\text{II}}(\mu\text{-O}_2\text{Cbiph})_3\text{Fe}^{\text{II}}(\mu\text{-O}_2\text{Cbiph})_3\text{Fe}^{\text{II}}\}$ units are capped either by four acetonitrile or THF ligands in **6** and **7**, respectively, or by two dimethoxyethane (**8**) molecules that

(46) Marchetti, F.; Marchetti, F.; Melai, B.; Pampaloni, G.; Zacchini, S. *Inorg. Chem.* **2007**, *46*, 3378–3384.

(47) Viertelhaus, M.; Adler, P.; Clérac, R.; Anson, C. E.; Powell, A. K. *Eur. J. Inorg. Chem.* **2005**, 692–703.

(48) Singh, B.; Long, J. R.; Fabrizi de Biani, F.; Gatteschi, D.; Stavropoulos, P. *J. Am. Chem. Soc.* **1997**, *119*, 7030–7047.

(49) (a) Meng, H.; Li, G.-H.; Xing, Y.; Yang, Y.-L.; Cui, Y.-J.; Liu, L.; Ding, H.; Pang, W.-Q. *Polyhedron* **2004**, *23*, 2357–2362. (b) Chang, W.-J.; Lin, H.-M.; Lii, K.-H. *J. Solid State Chem.* **2001**, *157*, 233–239.

(50) Choudhury, A.; Natarajan, S.; Rao, C. N. R. *J. Solid State Chem.* **1999**, *146*, 538–545.

(51) Gorun, S. M.; Lippard, S. J. *Inorg. Chem.* **1988**, *27*, 149–156.

(52) Holm, R. H.; Kennepohl, P.; Solomon, E. I. *Chem. Rev.* **1996**, *96*, 2239–2314.

(53) (a) Peterson, M. R.; Csizmadia, I. G. *J. Am. Chem. Soc.* **1979**, *101*, 1076–1079. (b) Gandour, R. D. *Bioorg. Chem.* **1981**, *10*, 169–176. (c) Rebeck, J., Jr.; Duff, R. J.; Gordon, W. E.; Parris, K. *J. Am. Chem. Soc.* **1986**, *108*, 6068–6069.

(54) Whittington, D. A.; Lippard, S. J. *J. Am. Chem. Soc.* **2001**, *123*, 827–838.

(55) Rinaldo, D.; Philipp, D. M.; Lippard, S. J.; Friesner, R. A. *J. Am. Chem. Soc.* **2007**, *129*, 3135–3147.

Table 4. Pertinent Structural Parameters for 1–8

$\tau = \alpha - \beta = \text{tilt}$

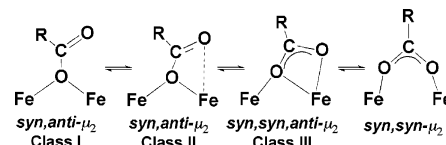
	1	2	3	4a	5	6a	7	8	MMOH ^b		
									[Fe(O ₂ CH) ₂ • 1/3HO ₂ CH] _n ^a	protomer A	protomer B
Fe ^{non} –Fe ^{1_int}	3.4658(6)	3.4266(7)	3.4579(15)	3.402[13]	3.4569(9)	3.5790(6)	3.565 [22]	3.606(3)	3.1973(10)	3.31	3.27
A (Å)	2.0841(12)	2.0845(16)	2.082(2)	2.075[1]	2.0775(18)	2.160(1)	2.202[18]	2.153(2)	2.145(4)	2.44	2.31
B (Å)	2.1997(12)	2.2131(16)	2.196(2)	2.229[1]	2.2783(19)	2.2915(14)	2.265[20]	2.2238(19)	2.134(4)	2.45	2.26
C (Å)	2.0821(13)	2.1193(16)	2.075(2)	2.059[1]	2.0772(18)				2.072(4)		
D (Å)	3.3688(13)	3.4508(16)	3.3413(22)	3.440[22]	3.5266(19)	2.1155(15)	2.124[19]	2.192(2)	3.506	2.44	2.37
α (deg)	124.98(11)	125.87(14)	125.99(19)	127.44[30]	124.57(17)	130.01(12)	152.0[38]	131.92(13)	127.91	130.81	144.94
β (deg)	126.86(11)	128.30(14)	126.16(18)	128.01[81]	129.72(16)	85.82(11)	86.41[90]	89.00(13)	133.21	91.23	92.75
γ (deg)	68.88(9)	66.92(12)	69.26(16)	67.60[48]	67.40(15)	94.03(12)	93.28[88]	90.94(12)	63.08	91.82	88.05
θ (deg)	107.97(5)	105.71(7)	107.84(9)	104.39[62]	104.96(7)	106.99(6)	105.9[22]	110.93(8)	96.71(16)	85.26	91.10
τ = α – β (deg)	–1.88	–2.43	–0.17	–0.57	–5.15	44.19	65.59	42.92	–5.30	39.58	52.19
category ^c	class 1	class 1	class 1	class 1	class 1	class 3	class 3	class 3	class 1		

^a Reference 47; the values for the {Fe₂(μ-1,1-O₂CH)₂(μ-1,3-O₂CH)} unit are listed. ^b Reference 54 from PDB code 1FYZ on MMOH_{red} at 2.15 Å resolution; measurements taken in *Coot* modeling software. ^c Classification according to ref 59.

render the terminal iron atoms hexacoordinate. The Fe–N bond distances and C–N triple bond lengths of 1.137(3) and 1.116(3) Å in **6a** are similar to those previously reported for iron(II) acetonitrile complexes.^{21,22} The Fe–N≡C angles of 173.85(18) and 159.1(2)° are slightly bent, and the N≡C–C angles are essentially linear at 179.5(3) and 177.3(3)°. The remaining bond distances for the carboxylate ligands to the iron centers in **6–8** lie between 1.977(3) and 2.2847(14) Å (Table 3). The monoatomic-bridged carboxylate motif has been previously observed in diferrous compounds. An example is [Fe₂(μ-L)(μ-O₂CR)(O₂CR)(N)₂], where L is a dinucleating bis(carboxylate) ligand based on *m*-xylylenediamine bis(Kemp's triacid imide) and N is a *py*- or imidazole-derived ligand.⁵⁶ Others include those in polymeric complexes, such as {[Fe(μ-O₂CH)₂]_{1/3}HO₂CH]_n,⁴⁷ and the MMOH active site.⁵⁴ In addition, similar linear triiron arrays occur in acetate-bridged complexes, e.g., [Fe^{II}₃(μ-O₂CMe)₆(BIPhMe)₂] [BIPhMe = 2,2'-bis(1-methylimidazolyl)(phenyl)methoxymethane]⁵⁷ and (Et₄N)₂[Fe^{II}₃(μ-OAc)₈],⁵⁸ the structures of which have been thoroughly described.⁵⁷

The monoatomic bridging motif of carboxylate ligands has been studied in detail, leading to the definition of the “carboxylate shift”.⁵⁹ Compounds with a monoatomic carboxylate bridge can be grouped into three categories depending on several parameters. Class 3 compounds are defined

Chart 4



by a strong interaction between the *dangling* oxygen atom (O_d in Table 4; O(2) in the X-ray nomenclature in Figures 3 and 6) and the interacting iron center (Fe^{1_int}), resulting in relatively large Fe–Fe distances and a tilt value τ around 50° (for the definition of the tilt angle τ , see Table 4). Conversely, class 1 compounds have essentially no or very weak interactions between O_d and Fe^{1_int}, resulting in shorter Fe–Fe distances and $\alpha \sim \beta$. Class 2 compounds are grouped in between and are characterized by a weak Fe^{1_int}...O_d interaction. Compounds **6–8** with mean Fe–Fe and Fe–O_d distances of 3.383[12] and 2.144[24] Å, respectively, fall into class 3. Complexes **1–5** belong to class 1 because they have significantly shorter Fe–Fe distances, 3.442[12] Å, and longer Fe^{1_int}–O_d contacts, 3.426[33] Å. The class 1 configuration of **1–5** allows atom O_d to interact with another metal atom, Fe^{2_int}, and ultimately results in the observed *dimer of dimers* structures. The interconversion of purely syn,anti-μ₂-1,1- (class 1), syn,syn,anti-μ₂-3,1,1- (class 3), and syn,syn-μ₂-1,3-bridging modes is shown in Chart 4.

The structures of compounds **9** and **10** are shown in Figure 7, and selected bond lengths and angles are provided in Table 3. There are two crystallographically equivalent square-pyramidal iron atoms and four bridging carboxylate ligands. The average Fe–Fe and Fe–N distances of 2.913[22] and 2.106[12] Å, respectively, compare well with those in previously reported diiron(II) paddlewheel compounds. The Fe–Fe and Fe–N distances of [Fe₂(μ-O₂CAr^{Tol})₄(4^{-t}Bupy)₂]²⁷

(56) LeCloux, D. D.; Barrios, A. M.; Mizoguchi, T. J.; Lippard, S. J. *J. Am. Chem. Soc.* **1998**, *120*, 9001–9014.

(57) (a) Rardin, R. L.; Bino, A.; Poganiuch, P.; Tolman, W. B.; Liu, S.; Lippard, S. J. *Angew. Chem., Int. Ed.* **1990**, *29*, 812–814. (b) Rardin, R. L.; Poganiuch, P.; Bino, A.; Goldberg, D. P.; Tolman, W. B.; Liu, S.; Lippard, S. J. *J. Am. Chem. Soc.* **1992**, *114*, 5240–5249.

(58) Reynolds, R. A., III; Dunham, W. R.; Coucouvanis, D. *Inorg. Chem.* **1998**, *37*, 1232–1241.

(59) Rardin, R. L.; Tolman, W. B.; Lippard, S. J. *New J. Chem.* **1991**, *15*, 417–430.

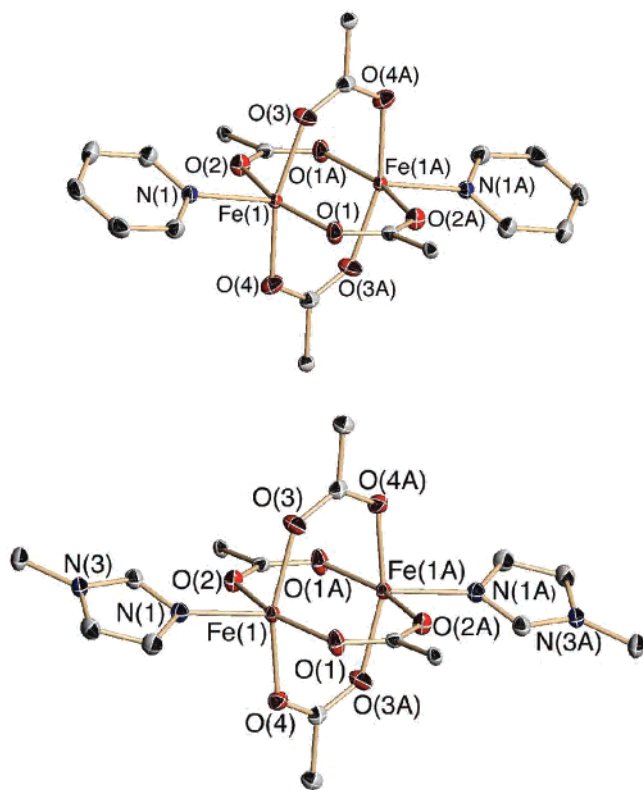


Figure 7. ORTEP diagrams of **9** (top) and **10** (bottom) showing 50% probability thermal ellipsoids for all non-hydrogen atoms. All atoms of the O_2Cbiph ligand, except for the carboxylate group and the α -carbon atom, were omitted for clarity.

and $[\text{Fe}_2(\mu\text{-O}_2\text{CPh})_4(\text{py})_2]\cdot\text{MeCN}^{60}$ are 2.8229(9) and 2.851(2) Å and 2.105(4) and 2.092(8) Å, respectively. The corresponding terphenylcarboxylate compounds $[\text{Fe}_2(\mu\text{-O}_2\text{CAR}^{\text{Toi}})_2(\text{O}_2\text{CAR}^{\text{Toi}})_2(\text{L})_2]$ (L = py or 1-Melm) crystallize with windmill structures.²⁷ Although a large number of paddlewheel compounds have been reported, diiron paddlewheel complexes are relatively scarce. Additional structural analyses of **1–10** including (i) a prediction of the Fe–O bond lengths based on bond valence sum analyses and (ii) the distribution of biphenylcarboxylate torsion angles, ϕ , with different structural composition, can be found in the Supporting Information.

Mössbauer Spectroscopy. The zero-field Mössbauer spectra of **2–4**, **6**, and **8–10** were recorded at 4.2 K in the absence of an external field, and the resulting parameters are listed in Table 5. The spectra of the high-spin diiron(II) complexes **9** and **10** display one sharp and symmetric quadrupole doublet, as is expected for two indistinguishable iron sites related by a center of symmetry (Figure 8). Complexes **6** and **8** contain two chemically distinguishable iron atoms, and quadrupole doublets in a 2:1 ratio are observed in the Mössbauer spectra for these triiron(II) compounds (Figure 8). This ratio allows for peak assignments, with the more intense, outer quadrupole doublet corresponding to the outer [terminal, Fe(1), and Fe(3)] iron atoms (Fe_o) and the inner doublet to the inner [center and

Table 5. Zero-Field Mössbauer Parameters at 4.2 K for Carboxylate-Rich Iron(II) Complexes **2–4**, **6**, and **8–10** and Related Enzyme Active Sites

compd	δ (mm s ⁻¹)	ΔE_Q (mm s ⁻¹)	Γ (mm s ⁻¹)	site ^a	CE ^b
2	1.16(2)	2.98(2)	0.25(2)	Fe_o	Sp, NO ₄
	1.14(2)	1.95(2)	0.26(2)	Fe_i	Sp, O ₅
3	1.17(2)	3.64(2)	0.23(2)	Fe_o	Sp, NO ₄
	1.17(2)	2.48(2)	0.29(2)	Fe_i	Sp, O ₅
4	1.17(2)	3.14(2)	0.26(2)	Fe_o	Sp, NO ₄
	1.18(2)	2.29(2)	0.30(2)	Fe_i	Sp, O ₅
6	1.27(2)	2.96(2)	0.32(2)	Fe_o	Oh, N ₂ O ₄
	1.36(2)	2.59(2)	0.28(2)	Fe_i	Oh, O ₆
8	1.30(2)	3.13(2)	0.33(2)	Fe_o	Oh, O ₆
	1.40(2)	2.67(2)	0.30(2)	Fe_i	Oh, O ₆
9	1.15(2)	2.88(2)	0.32(2)		Sp, NO ₄
10	1.13(2)	2.53(2)	0.24(2)		Sp, NO ₄
MMOH ^c	1.30	2.87			
MMOH ^d	1.3	2.4–3.1			
RNR-R2 ^e	1.26	3.13			
$\Delta 9D^f$	1.30	3.04–3.36			

^a Fe_o = terminal (outer) iron; Fe_i = central (inner) iron. ^b CE = coordination environment (geometry and donor set); Sp = square pyramidal; Oh = octahedral. ^c *Methylococcus capsulatus* (Bath). Liu, K. E.; Valentine, A. M.; Wang, D.; Huynh, B. H.; Edmondson, D. E.; Salifoglou, A.; Lippard, S. J. *J. Am. Chem. Soc.* **1995**, *117*, 10174–10185. ^d *Methylosinus trichosporium* OB3b. Pulver, S.; Froland, W. A.; Fox, B. G.; Lipscomb, J. D.; Solomon, E. I. *J. Am. Chem. Soc.* **1993**, *115*, 12409–12422. ^e Coates Pulver, S.; Tong, W. H.; Bollinger, J. M.; Stubbe, J.; Solomon, E. I. *J. Am. Chem. Soc.* **1995**, *117*, 12664–12678. ^f Fox, B. G.; Shanklin, J.; Somerville, C.; Münck, E. *Proc. Natl. Acad. Sci. U.S.A.* **1993**, *90*, 2486–2490.

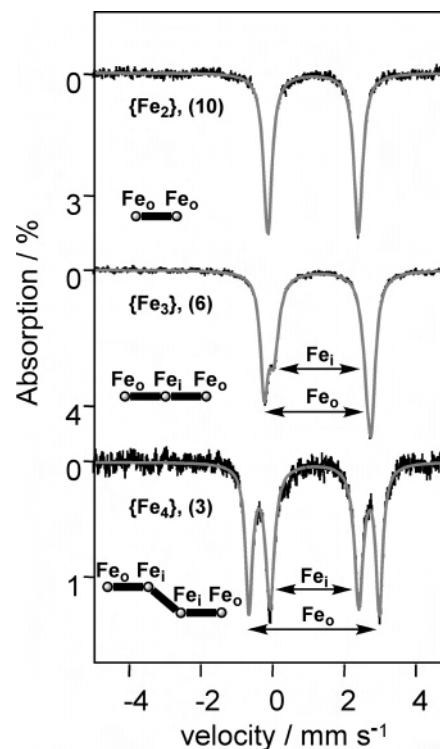


Figure 8. Zero-field Mössbauer spectra at 4.2 K [experimental data (I) and calculated fits (gray solid line)] for solid samples of **10** (top), **6** (middle), and **3** (bottom).

Fe(2)] iron atoms (Fe_i). The observed isomer shifts (δ) of 1.14[1] mm s⁻¹ for the pentacoordinate complexes **9** and **10** and 1.33[3] mm s⁻¹ for the hexacoordinate complexes **6** and **8** agree well with the trend expected for high-spin iron(II) complexes.^{5a}

The tetrairon(II) complexes **2–4** display two quadrupole doublets in a 1:1 ratio. Their assignments in Table 5 can be

(60) Randall, C. R.; Shu, L.; Chiou, Y.-M.; Hagen, K. S.; Ito, M.; Kitajima, N.; Lachicotte, R. J.; Zang, Y.; Que, L., Jr. *Inorg. Chem.* **1995**, *34*, 1036–1039.

rationalized by considering the isomer shift and quadrupole splitting (ΔE_Q) parameters. Both the degenerate two inner (Fe_i) and outer (Fe_o) absorption peaks produce a quadrupole doublet with an isomer shift in the expected range for pentacoordinate species, ca. 1.16 mm s^{-1} for the three complexes (Figure 8). If one inner peak and one outer peak formed a single quadrupole doublet, then δ values as low as 0.88 mm s^{-1} and as high as 1.46 mm s^{-1} would be obtained for **3**. Values lower than 1.0 and higher than 1.3 are very unlikely for pentacoordinate high-spin iron(II) species, and this assignment can therefore be excluded. Less obvious is the identification of the quadrupole doublets belonging to the terminal [Fe(1) and Fe(4)] and central [Fe(2) and Fe(3)] iron atoms in complexes **2–4**. However, the electric field gradient is expected to be higher for a more asymmetric NO_4 donor set than for an O_5 donor set when the iron atoms have comparable coordination environments. Indeed, both the terminal and central iron atoms have similar square-pyramidal coordination spheres with similar τ values (Table 3), justifying the assignment of the outer quadrupole doublet to the outer (terminal) iron atoms and the inner doublet to the inner (center) iron ions.

Magnetic Susceptibility Studies. Plots of the magnetic susceptibility (χ_M) and effective moment (μ_{eff}) versus temperature for **2–4**, **6**, and **8–10** are depicted in Figure 9 and in the Supporting Information; the μ_{eff} values are summarized in Table 6. The theoretical effective moments are $9.80 \mu_B$ for **2–4** with four independent $S = 2$ ions, $8.49 \mu_B$ for **6** and **8** with three independent $S = 2$ ions, and $6.93 \mu_B$ for **9** and **10** with two independent $S = 2$ ions and $g = 2.0$. The experimental effective moments at 300 K are consistent with these calculated values (Table 6). At low temperature, all compounds show a significant decrease in μ_{eff} relative to their values at 300 K. For complexes containing an even number of Fe^{II} ions (**2–4**, **9**, and **10**), fully antiparallel spin alignment would yield an effective moment of $0 \mu_B$. For the complexes with three Fe^{II} ions (**6** and **8**), the alignment would yield a spin-only value of $4.90 \mu_B$ (assuming for $g = 2.0$). All of these complexes approach their corresponding theoretical value, as shown in Table 6.

The magnetic properties of paddlewheel diiron and linear triiron complexes have been studied previously.²⁷ The two ferrous ions in the windmill complexes $[\text{Fe}_2(\mu\text{-O}_2\text{CAr}^{\text{Tot}})_2(\text{O}_2\text{CAr}^{\text{Tot}})_2(\text{py})_2]$ and $[\text{Fe}_2(\mu\text{-O}_2\text{CAr}^{\text{Tot}})_2(\text{O}_2\text{CAr}^{\text{Tot}})_2(1\text{-MeIm})_2]$ and in the paddlewheel complex $[\text{Fe}_2(\mu\text{-O}_2\text{CAr}^{\text{Tot}})_4(4\text{-}^i\text{Bupy})_2]$ are antiferromagnetically coupled. The exchange coupling constants (J ; the J formalism is used here, $\mathbf{H} = JS_iS_j$, rather than $-2J$ or $-J$) for the windmill complexes were determined to be $\sim 2 \text{ cm}^{-1}$ for the py and 1-MeIm species. However, zfs was not accounted for when fitting these data.²⁷ Intramolecular ferro- and antiferromagnetic interactions occur in linear triiron(II) complexes depending on the interaction of the dangling oxygen of the second oxygen from the monobridging carboxylate.¹⁷ The magnetic properties correlate with structural parameters. The compounds $[\text{Fe}_3(\text{OAc})_6(\text{BIPhMe})_2]$, $[\text{Fe}_3(\text{OAc})_6(\text{BIPhOH})_2]$ [$\text{BIPhOH} = \text{bis}(1\text{-methyl-2-imidazolyl})\text{phenylhydroxymethane}$], and $[\text{Fe}_3(\text{OAc})_6(\text{BIDPhEH})_2]$ [$\text{BIDPhEH} =$

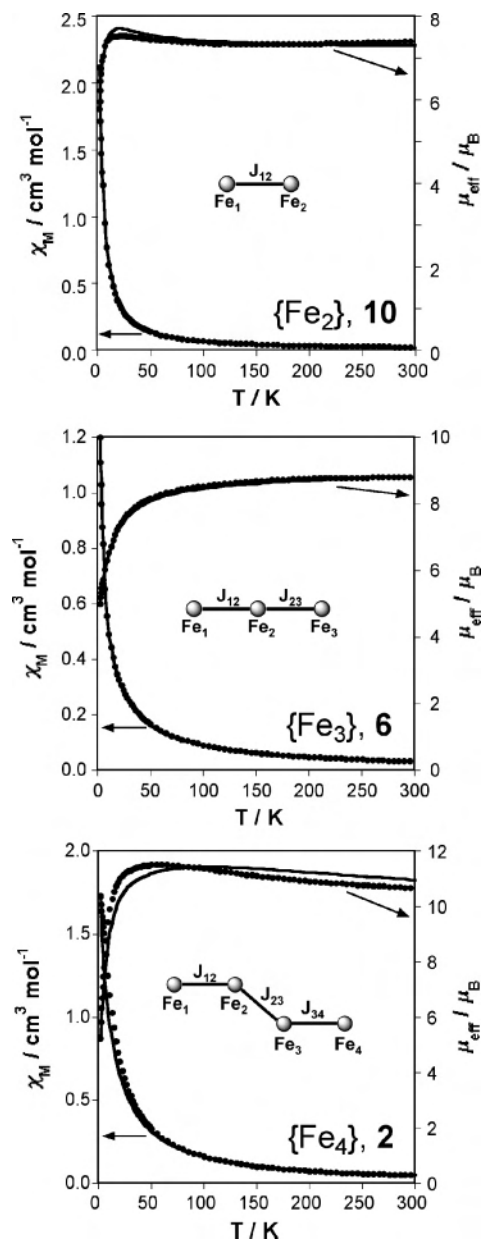


Figure 9. Plot of experimental data (\bullet) and theoretical fits (solid line) of molar susceptibility, χ_M , and effective moment, μ_{eff} , for **10** (top), **6** (middle), and **2** (bottom): $J = 0.15 \text{ cm}^{-1}$, $D = -9 \text{ cm}^{-1}$, $g_{\perp} = 1.7$, and $g_{\parallel} = 2.7$ for **10**; $J_{12} = J_{23} = 1.8 \text{ cm}^{-1}$, $D_1 = D_3 = -1.0 \text{ cm}^{-1}$, $D_2 = -17 \text{ cm}^{-1}$, $g_{1,\text{iso}} = g_{3,\text{iso}} = 2.13$, and $g_{2,\text{iso}} = 1.95$ for **6**; $J_{12} = J_{34} = 2.26 \text{ cm}^{-1}$, $J_{23} = -50 \text{ cm}^{-1}$, $D = 0$, and $g_{\text{iso}} = 2.32$ for **2**.

1,1-bis(1-methyl-2-imidazolyl)-1-(3,5-di-*tert*-butyl-4-hydroxyphenyl)ethane], grouped into class 1 (see above), show a parallel spin alignment ($J = -2$ to -5 cm^{-1}). Complexes $[\text{Fe}_3(\text{O}_2\text{CPh})_6(\text{PrOx})_2]$ [$\text{PrOx} = \text{bis}[2\text{-}((4S)\text{-}(1\text{-methylethyl})\text{-}1,3\text{-oxazoliny])\text{methane}]$] and $[\text{Fe}_3(\text{O}_2\text{CPh})_6(\text{PheMeEda})_2]$ [$\text{PheMeEda} = N,N,N'$ -trimethyl- N' -[4,4-dimethyl-4-(3,5-di-*tert*-butyl-4-hydroxyphenyl)butyl]ethylenediamine], both of which are in class 3, display antiferromagnetic coupling ($J \sim 1 \text{ cm}^{-1}$).¹⁷ The antiferromagnetic behavior of class 3 compounds **6–8** (Tables 4 and 6) is in agreement with these results.

Quantitative Analysis of the Magnetic Data. (a) Dinuclear Complexes 9 and 10. In principle, these complexes should exhibit magnetic behavior that is easiest to interpret

Table 6. Summary of Susceptibility Data for Complexes **2–4**, **6**, and **8–10**

complex	μ_{eff} at $T_{\text{min}}^a/\mu\text{B}$	μ_{eff} at $T_{\text{max}}^b/\mu\text{B}$
Planar Tetrairon(II) Complexes		
calcd ^c for AF coupling	0 ^d	9.80 ^e
2	4.2	10.6
3	2.0	10.6
4	1.5	9.89
Linear Triiron(II) Complexes		
calcd ^c for AF coupling	4.90 ^f	8.49 ^g
6	4.99	8.81
8	5.09	9.26
Paddlewheel Diiron(II) Complexes		
calcd ^c for AF coupling	0 ^d	6.93 ^h
9	0.4	6.99
10	3.1	7.27

^a The minimum temperature is 2 K. ^b The maximum temperature is 300 K. ^c Calculated with $\mu_{\text{eff}} = [g^2S(S+1)]^{1/2}$ with $g = 2.0$. ^d Total spin $S = 0$. ^e Four independent $S = 2$ ferrous ions. ^f Total spin $S = 2$. ^g Three independent $S = 2$ ferrous ions. ^h Two independent $S = 2$ ferrous ions.

because they are the simplest spin systems among those described herein, with only one exchange coupling parameter and two ions with presumed symmetry equivalence. The temperature-dependent susceptibility behavior for **10** can be described solely by a model including single-ion zfs without exchange coupling, yielding $D_i \approx -4.5 \text{ cm}^{-1}$ (a negative value is more successful than positive D_i) with $g_{\text{iso}} \approx 2.1$, values consistent with single Fe^{II} ions in these environments.¹⁹ This model accounts for the high-temperature plateau of μ_{eff} and for its sharp drop at low temperature ($T < 20 \text{ K}$; Figure 9). However, the model does not explain the slight “bump” in μ_{eff} seen near 30 K. Inclusion of exchange coupling improves the fit, although this improvement may simply reflect the increase in the parameters. Taken at face value, such fits yield $J \approx 0.1\text{--}0.2 \text{ cm}^{-1}$, with zfs again reasonable for the single ions, $D_i \approx -9 \text{ cm}^{-1}$. Inclusion of exchange coupling does not reproduce the “bump” near 30 K. Inclusion of g -value anisotropy reproduces this feature to a slight extent, resulting in $g_{\perp} \approx 1.75\text{--}(5)$ and $g_{\parallel} \approx 2.65\text{--}(2)$. This spread is much larger than expected, and the low value for g_{\perp} may not be realistic, although the average (g_{avg}) is 2.05. Inclusion of temperature independent paramagnetism (TIP) and/or a small amount of Fe^{III} impurity has little effect on the overall fit quality.

The situation with complex **9** is dramatically different. Qualitatively, the decrease in μ_{eff} versus T (Supporting Information) is indicative of antiferromagnetic coupling between the two Fe^{II} ions. However, the shape of the curves is unlike that seen for typical paramagnets (vide supra). The magnetic data for this complex proved surprisingly difficult to analyze quantitatively. As might be expected, it was impossible to fit the data with only exchange coupling between the two Fe^{II} ions, whereas the use of only zfs (i.e., no exchange coupling) was also unsuccessful, in contrast to **10**. The combination of these effects did not improve matters much. In many fit attempts with the use of an isotropic g value, the fit maximum was generally reached for this parameter. The use of axial g values led to their divergence, resulting in both unrealistically large and small values, generally the allowed fit extrema. Correction factors such as TIP and inclusion of an Fe^{III} impurity generally had a

negligible effect on the fit quality. The only moderately successful fits, as defined by both matching the data and yielding believable single-ion parameters, were those in which either the exchange coupling was allowed to be anisotropic (uniaxial) or the zfs axes were noncollinear. The latter cases typically yielded $J \approx 22 \text{ cm}^{-1}$, $D_i \approx -8 \text{ cm}^{-1}$, $g_{\text{iso}} \approx 2.3$, and with D_2 rotated with respect to D_1 by Euler angles α and $\beta \approx 45^\circ$, which yielded a very rhombic zfs. Regardless of the exact magnitude of the magnetic parameters in the two complexes, there was a dramatic difference between the two. There is strong antiferromagnetic coupling in **9**, which may be very anisotropic, whereas in **10**, the two Fe^{II} ions are almost noninteracting. That such a difference results solely from the difference in axial ligation, with ligands differing relatively little as donors (py and 1-MeIm), is truly remarkable, and at this point, we have no explanation for the observation.

(b) Trinuclear Complexes 6 and 8. In these complexes, the physical model becomes far more complicated because there are potentially three exchange coupling constants (J_{12} , J_{13} , and J_{23}) that could be anisotropic and there are similarly three zfs systems that could have any orientation with respect to each other. To make the problem at all tractable, we imposed the symmetry constraint that the single-ion parameters for the two terminal Fe^{II} ions be identical, which is supported by the structural and Mössbauer data given above. We also disregarded any noncollinearity of the zfs coordinates for these ions. Last, we considered only exchange coupling between adjacent ions and related these by symmetry as well so that $J_{12} \equiv J_{23}$ and $J_{13} \equiv 0$.

Complexes **6** and **8** exhibit qualitatively the same magnetic susceptibility behavior (Figure 9 and the Supporting Information), namely, a decrease in μ_{eff} (or χT) as T decreases. A reasonable fit is obtained for **6** with the use of $J_{12} = J_{23} \approx 1.8\text{--}(2) \text{ cm}^{-1}$, $g_{\text{iso}}(\text{Fe}_{1,3(\text{o})}) \approx 2.13\text{--}(3)$, $g_{\text{iso}}(\text{Fe}_{2(\text{i})}) \approx 1.95\text{--}(5)$, $D(\text{Fe}_{1,3(\text{o})}) \approx -1.0\text{--}(5)$, and $-1 > D(\text{Fe}_{2(\text{i})}) > -18 \text{ cm}^{-1}$. The fit value for $D(\text{Fe}_2)$, in contrast to the other parameters, is highly variable; it is very sensitive to initial parameters and to the inclusion of the additional terms, TIP and/or the amount of Fe^{III} impurity, despite the fact that neither is large [e.g., TIP $\approx (1\text{--}4) \times 10^{-3}$; mole fraction of Fe^{III} ≈ 0.07 , a value that can hardly be considered as equivalent to an analytical impurity but merely a fit result]. Complex **8** was analyzed first with the use of a model in which all three Fe^{II} ions were held equivalent. In this model, the exchange coupling ($J_{12} = J_{23} \approx 1.5 \text{ cm}^{-1}$) is quite small and the zfs of each single ion is negligible ($D_i < 0.01 \text{ cm}^{-1}$). Indeed, a fit with only exchange coupling is reasonably successful, yielding $J_{12} = J_{23} \approx 1.7 \text{ cm}^{-1}$ and $g_{\text{iso}} \approx 2.3$. The more physically meaningful model, where the outer Fe^{II} ions are held the same but the inner Fe^{II} ion is allowed to differ, may suffer from too broad a parameter space but did give results for **8** resembling those for **6**, at least in terms of exchange coupling, although with much lower precision: $J_{12} = J_{23} \approx 1.2\text{--}(2) \text{ cm}^{-1}$, $g_{\text{iso}}(\text{Fe}_{1,3(\text{o})}) \approx 1.9\text{--}(1)$, $g_{\text{iso}}(\text{Fe}_{2(\text{i})}) \approx 2.4\text{--}(2)$, $D(\text{Fe}_{1,3(\text{o})}) \approx -10\text{--}(5)$, and $1 < |D(\text{Fe}_{2(\text{i})})| < 20 \text{ cm}^{-1}$ (a negative value for $D(\text{Fe}_{2(\text{i})})$ yields slightly better fits, but a positive value cannot be ruled out).

One must be circumspect about the quantitative aspects of these fits, yet it is clear that, in these trinuclear complexes, there is very little exchange coupling. It also appears that the zfs of the outer Fe ions is relatively small, whereas that of the central ion may be larger. The Fe^{II} ions in **8** have an O₆ donor set, and in **6**, it is O₄N₂ but the N donor is the weak ligand MeCN. Such a symmetrical environment might lead to small zfs, although this may be a coincidence. The complex [Fe(Im)₆](NO₃)₂, with an N₆ donor set, has very large zfs ($D \approx 20 \text{ cm}^{-1}$), which is poorly described by an $S = 2$ spin Hamiltonian. A full ligand-field treatment is needed.⁶¹

(c) Tetranuclear Complexes 2–4. These complexes present a very difficult case for the quantitative analysis of magnetic susceptibility behavior, and we are not aware of others who have attempted to extract a full set of spin Hamiltonian parameters. The outer Fe ions of the tetranuclear complexes (**2–4**) are structurally very similar to those in the diiron complexes **9** and **10**. This result suggests that the single-ion parameters of these outer Fe ions would resemble those of the dinuclear Fe ions, which should facilitate fitting of the magnetic data of the more complex tetrairon systems. Unfortunately, the fit results for **9** and **10** are quite different, which suggests that the nature of the terminal N-donor ligand is crucial in determining both the single-ion properties and the exchange coupling. Complexes **2–4** also differ in their axial ligands so that generalization of single-ion parameters among these complexes may not be justified. Consistent with an axial ligand effect, **3** and **4** exhibit significantly different magnetic behavior (see the Supporting Information) despite their axial ligands differing by only methyl groups. As described above, there are six exchange coupling constants; however, these will be simplified by the assumption of no coupling between nonadjacent ions and symmetrical coupling between terminal and internal ions, so that $J_{12} \equiv J_{34} \neq J_{23} \neq 0$ and $J_{13} = J_{14} = J_{34} = 0$. In principle, the single-ion parameters for the terminal ions, Fe_{1,4}, should be equivalent, as should those for the internal ions, Fe_{2,3}, but the internal and terminal ions need not be equivalent (see the Mössbauer data above). In practice, however, in order to restrict the parameter space, we employed two approaches: in one case, we kept all of the parameters for the single ions equivalent; in the other case, we kept the parameters for the terminal Fe^{II} ions the same as those in **10**: $-8 > D > -10 \text{ cm}^{-1}$ and $2.0 < g_{\text{iso}} < 2.1$, which are representative for Fe^{II}. We did not consider anisotropy or noncollinearity among these Fe^{II} ions. The results described here are not definitive but at least shed some light on the magnetic interactions within these complicated multinuclear systems. The magnetic susceptibility data for these complexes are shown in Figure 9 and in the Supporting Information. All of them exhibit qualitatively the same behavior, with a gradual decrease in μ_{eff} (or χT) as T decreases. Complexes **2** and **3**, however, display an inflection at $\sim 10 \text{ K}$ that is absent in the data for **4**.

For **2**, it was possible to fit the data moderately well with a parameter set excluding zfs. The results indicate antifer-

romagnetic coupling between the terminal (outer) and internal (inner) ions but strong ferromagnetic coupling between the internal ions: $J_{12} = J_{34} \approx 2.3 \text{ cm}^{-1}$, $J_{23} \approx -50 \text{ cm}^{-1}$, and $g_{\text{iso}} \approx 2.3$. For complex **3**, all of the coupling was antiferromagnetic: $J_{12} = J_{34} \approx 3.8 \text{ cm}^{-1}$, $J_{23} \approx 14 \text{ cm}^{-1}$, and $g_{\text{iso}} \approx 2.3$. Relatively small values for exchange coupling between inner and outer Fe ions are consistent with the results for the dinuclear complex **10**, which represent the “dimer”, whereas **2** and **3** are the *dimer of dimers*.

Complex **4** presented the least successful situation, in that in all cases the fits required unrealistically large g values ($g > 3.0$). This situation was obtained even with inclusion of zfs, for which the fit yielded negligibly small values ($D_i < 0.05 \text{ cm}^{-1}$). When the g values were disregarded, the fits invariably yielded large magnitude antiferromagnetic coupling of internal to terminal ions [$J_{12} = J_{34} \approx 60(20) \text{ cm}^{-1}$] but smaller magnitude ferromagnetic coupling between the internal ions [$J_{23} \approx 5(3) \text{ cm}^{-1}$]. Complex **4** would thus seem to resemble the diiron complex **9**, in terms of strong exchange coupling within the “dimer”.

The use of single-ion parameters as described above for the terminal Fe^{II} ions was moderately successful in fitting data for **2** and **3**, but this model was totally unsuccessful for **4**, providing additional evidence as to the impenetrable nature of its magnetic behavior. Qualitatively, it is possible that there is a combination of ferro- and antiferromagnetic exchange interactions in these tetranuclear high-spin Fe^{II} clusters because this situation occurs in iron–sulfur proteins.⁶² A key difference between the systems studied here versus proteins and model compounds containing Fe₄S₄ clusters is the symmetrical linkage (via bridging sulfides) of all Fe ions with each other and their roughly equivalent coordination spheres.

Electrochemistry. The CVs of the diiron(II) complexes **9** and **10** in 0.50 M ⁿBu₄N(PF₆)/CH₂Cl₂ solutions collected at a scan rate of 0.20 V s⁻¹ display one quasireversible oxidation wave (Figure 10), I^{ox}, which is assigned⁶³ to an Fe^{II}Fe^{II} → Fe^{II}Fe^{III} oxidation. The redox potentials [$E_{1/2} = (E_{\text{p,a}} + E_{\text{p,c}})/2$] of 0.02 and -0.32 V for **9** and **10**, respectively, are comparable with that of [Fe₂(μ -O₂CAR^{Tol})₄(^tBupy)₂], -0.22 V vs Cp₂Fe⁺/Cp₂Fe, and agree well with the expected⁶⁴ net electron-donor character of the exogenous N-donor ligands: 1-MeIm > *tert*-butylpyridine > py. In contrast to [Fe₂(μ -O₂CAR^{Tol})₄(^tBupy)₂]⁺, the mixed-valent oxidation products of **9** and **10** have an $I_{\text{p}}^{\text{red}}/I_{\text{p}}^{\text{ox}}$ ratio for I^{ox} of 0.3 and 0.4 at 0.20 V s⁻¹, respectively, indicating incomplete chemical reversibility. At lower scan rates, the $I_{\text{p}}^{\text{red}}/I_{\text{p}}^{\text{ox}}$ ratio decreases and approaches zero for **9** at scan rates lower than 50 mV s⁻¹. Upon potential scan reversal following the formation of wave I^{ox}, one quasireversible reduction wave, II^{red}, at -0.55 (**9**) and -0.73 V (**10**) vs Cp₂Fe⁺/Cp₂Fe was detected, which we attribute to the reduction of products formed in the anodic process at I^{ox}

(62) Noodleman, L.; Peng, C. Y.; Case, D. A.; Mouesca, J.-M. *Coord. Chem. Rev.* **1995**, *144*, 199–244.

(63) Lee, D.; Krebs, C.; Huynh, B. H.; Hendrich, M. P.; Lippard, S. J. *J. Am. Chem. Soc.* **2000**, *122*, 5000–5001.

(64) (a) Lever, A. B. P. *Inorg. Chem.* **1990**, *29*, 1271–1285. (b) Pombeiro, A. J. L. *Eur. J. Inorg. Chem.* **2007**, 1473–1482.

(61) Carver, G.; Tregenna-Piggott, P. L. W.; Barra, A.-L.; Neels, A.; Stride, J. A. *Inorg. Chem.* **2003**, *42*, 5771–5777.

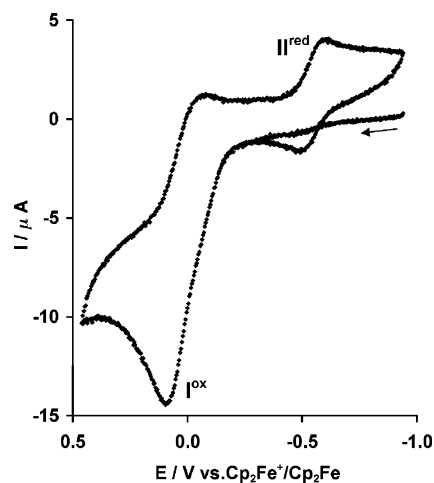


Figure 10. CV of 2 mM solutions in CH_2Cl_2 with 0.5 M $n\text{Bu}_4\text{N}(\text{PF}_6)$ of **9** at a platinum working electrode at a scan rate of 0.20 V s^{-1} . The $\text{Fe}^{\text{II}}\text{Fe}^{\text{II}} \rightarrow \text{Fe}^{\text{II}}\text{Fe}^{\text{III}}$ redox process is indicated by I^{ox} , and upon scan reversal after the oxidation process, the appearance of a new partially reversible species, II^{red} , is observed.

(Figure 10). It is assumed that the less sterically hindered biphenylcarboxylate ligand allows for a structural rearrangement upon oxidation that results in only partial reversibility of wave I, which is not seen in the CV of the more sterically shielded $[\text{Fe}_2(\mu\text{-O}_2\text{CAr}^{\text{Tol}})_4(\text{Bupy})_2]^+$. Only negligible geometric changes were observed for $[\text{Fe}^{\text{II}}_2(\mu\text{-O}_2\text{CAr}^{\text{Tol}})_4(\text{t-Bupy})_2]$ upon one-electron oxidation to the corresponding $\text{Fe}^{\text{II}}\text{Fe}^{\text{III}}$ species, as revealed by X-ray crystallography.⁶³ The triiron(II) complex **6** under the same experimental conditions in MeCN displayed one quasireversible ($E_{1/2} = -0.36 \text{ V}$) oxidation wave (see the Supporting Information), which became irreversible in CH_2Cl_2 , indicating oxidative decomposition due to loss of MeCN ligands and complex rearrangement. In addition, one irreversible ($E_p = -0.10 \text{ V}$ vs $\text{Cp}_2\text{Fe}^+/\text{Cp}_2\text{Fe}$) oxidation wave was observed. Scan reversal upon the first oxidation wave showed the appearance of one irreversible reduction wave at -0.85 V vs $\text{Cp}_2\text{Fe}^+/\text{Cp}_2\text{Fe}$.

Conclusion

A series of oligonuclear iron(II) complexes containing flexible and asymmetric 2-phenylbenzoate ligands with three different structural motifs were prepared and thoroughly characterized. Included are (i) the novel planar tetrairon(II) *dimer of dimers* complexes **1–5** with an unprecedented strong axial interaction between the two dimer subunits, (ii) the linear triiron(II) complexes **6–8**, and (iii) the paddlewheel diiron(II) complexes **9** and **10**. The steric pocket of the biphCO_2^- ligand allows for the isolation of discrete oligomers by preventing polymerization. Transition-metal complexes usually have a preferred coordination mode for carboxylate

ligands, which precludes the isolation of a large variety of structural motifs. Furthermore, the commonly favored syn-coordination mode normally prevents strong *dimer of dimers* interactions for non-ferrous paddlewheel associations. The iron carboxylate complexes described in this study have avoided this situation, and their structural diversity can be attributed to the flexible biphenylcarboxylate ligand and the easily accessible syn- and anti-binding modes of the carboxylates at the ferrous centers. Flexibility of carboxylate ligands in a biological context is thought to be an important factor for the proper function of non-heme diiron enzymes. The complexes were investigated by variable-temperature magnetic susceptibility studies, which showed a degree of intramolecular antiferromagnetic exchange coupling at low temperatures. Quantitative analysis of this phenomenon was very difficult because of the complex electronic structures of the constituent high-spin Fe^{II} ions. However, it appears that, in most cases, there is relatively weak antiferromagnetic exchange coupling between adjacent ions, $0 < J \leq 5 \text{ cm}^{-1}$, despite the extensive carboxylate bridging between them. Exceptions are the diiron complex **9**, which exhibits relatively strong antiferromagnetic coupling ($J > 20 \text{ cm}^{-1}$) yet is structurally almost the same as complex **10**, and the tetrairon complex **4**, in which there is likely also strong coupling between dimer units. The magnetic properties depend on effects that we cannot identify, and similarity in the coordination environment is not a sufficient determinant of these properties. Possibly, differences in the internal packing of the ligands, which give rise to disparate Fe–O bond lengths for the bridging carboxylates, are an important factor. A full understanding of the relationship between the structure and magnetism of oligomeric high-spin Fe^{II} ions remains to be determined.

Acknowledgment. This work was supported by Grant GM032134 from the National Institute of General Medical Sciences. E.R. is the recipient of a Schrödinger fellowship (Grant J2485-B10) from the Austrian Science Foundation. We thank Ms. Simone Friedle for assistance in acquiring the Mössbauer spectra and Dr. Sebastian Stoian for helpful discussions.

Supporting Information Available: Structural details, crystallographic tables, ORTEP diagrams with atom-numbering schemes, and X-ray crystallographic files in CIF format for complexes **1–11**, IR spectra for **1–10**, Mössbauer spectra of **2**, **4**, **8**, and **9**, magnetic plots of **3**, **4**, **8**, and **9**, CV of **6** in MeCN, and time-resolved UV–vis spectra of the oxygenation of **9**. This material is available free of charge via the Internet at <http://pubs.acs.org>.

IC701663J